PHOTOVOLTAIC PERFORMANCE OF PLATINUM-GRAPHENE BASED COUNTER ELECTRODE FOR DYE SENSITIZED SOLAR CELLS

MICHAEL NG'ENO KIPLANG'AT

MASTERS OF SCIENCE

(Physics)

JOMO KENYATTA UNIVERSITY

OF

AGRICULTURE AND TECHNOLOGY

2025

Photovoltaic Performance of Platinum-Graphene Based Counter Electrode for Dye Sensitized Solar Cells

Michael Ng'eno Kiplang'at

A Thesis Submitted in Partial Fulfillment of the Requirements for the Degree of Masters of Science in Physics of the Jomo Kenyatta University of Agriculture and Technology

2025

DECLARATION

This thesis is my original work and has not been presented for a degree in any other University

Signature……Date……..

Michael Ng'eno Kiplang'at

This thesis has been submitted for examination with our approval as the University Supervisors

Signature……Date……..

Dr. Waweru Simon Mugo, PhD

JKUAT, Kenya

Signature……Date……..

Dr. Timonah Nelson Soitah, PhD

JKUAT, Kenya

DEDICATION

I dedicate my entire work to my wife, Mrs. Cherono Ngeno and my dear mother, Mrs. Juliana Cheruiyot for their unending encouragement, support, unsurpassed efforts and love. Thank you so much for being so dear to me, I am proud of you. God bless you abundantly.

ACKNOWLEDGEMENT

I sincerely express special gratitude to my chief supervisor and guide Dr. Waweru Simon Mugo of Jomo Kenyatta University of Agriculture and Technology (JKUAT). I sincerely thank him for his unending will to be of help in the undertaking of this work. He has admirable knowledge in nanotechnology, thin film technology, and dye sensitized solar cells that are worth emulating. His great practical skills contributed properly to the success of my research. His discussions, critique and remarks greatly helped in the development of this work.

I am also grateful to my second supervisor Dr. Timonah Nelson Soita of JKUAT for his tireless encouragement and wise counsel.

I sincerely thank Dr. Anthony Kiroe, chairman physics department, JKUAT, for his encouragement and for providing the necessary facilities and working environment that enabled me accomplish this work. I am grateful to the technical and academic staff in physics department, JKUAT, for their support and words of encouragement during the course of research.

TABLE OF CONTENTS

LIST OF TABLES

LIST OF FIGURES

LIST OF SYMBOLS

η	Efficiency
I	Current
He	Helium
Ω/sq	Ohms/Square
e	Elementary charge
Pt	Platinum
ϕ	Photon flux
SnO_2:F	Fluorine doped Tin IV Oxide

LIST OF APPENDICES

ACRONYMS AND ABBREVIATIONS

AM	Air Mass
CE	Counter Electrode
DLG	Double Layer Graphene
DSSC	Dye Sensitized Solar Cell
DWCNTs	Doubled-Walled Carbon Nanotubes
E_f	Fermi Level
eV	Electron Volt
FTO	Fluorine-Doped Tin Oxide
Gr	Graphene
HOMO	High Occupied Molecular Orbital
K	Dirac Points
LUMO	Lowest Unoccupied Molecular Orbital
MLG	Multi-Layer Graphene
MWCTs	Multi-Walled Carbon Nanotubes
PCE	Power Conversion Efficiency
Pt/Gr	Platinum on Graphene
R_S	Sheet Resistance

SLG	Single-Layer Graphene
SLG	Single Layer Graphene
SP	Screen Printing
SWSNTs	Singled-Walled Carbon Nanotubes
UV-VIS -NIR	Ultraviolet-Visible-Near Infra-Red
WE	Working Electrode
Z	Impedence

ABSTRACT

Dye-sensitized solar cells (DSSCs) have emerged as new class of low cost energy conversion devices. DSSCs were fabricated using graphene on platinum-based counter electrodes, electrolyte and titanium dioxide thin films deposited on fluorine-doped tin oxide (FTO) using doctor blade technique. TiO_2 thin films as working electrode (WE's) were annealed at different rates; 2 ^{O}C/min, 1 ^{O}C/min, one step annealed and as deposited. Surface roughness and optical properties of TiO_2 thin films were examined using optical microscopy and UV-VIS spectroscopy respectively. Thin films annealed at low rate (1 ^{O}C/min) were found to have high transmittance, lower band gap energy and improved surface roughness for greater surface area for dye adsorption that resulted in better conversion efficiency of a solar cell. The prepared counter electrodes were characterized using UV-VIS spectrophotometry and four-point probe for optical transmittance and sheet resistance respectively. Transmittance of single layer, double graphene on platinum was found to be high (above 70 %) at visible wavelengths. It was found that each layer increase in graphene corresponds to decrease of 2.4 % in the optical transmittance of these films. Sheet resistance (R_s) was found to reduce with increase in number of graphene layers with 1100, 620 and 180 Ω/sq for single-layer (SLG), double layer (DLG) and multi-layer graphene (MLG) on FTO respectively. DSSCs were then characterized by analyzing the photocurrent-voltage characteristics. The results showed incorporation of SLG and DLG increase the short circuit current density and photoelectric conversion efficiency (η). However, incorporation of MLG led to reduction of η. Pt on SLG, Pt on DLG and Pt on MLG CE's had a conversion efficiency of 3.30, 3.41 and 2.16 % respectively. Pt on double Layer-Gr based CEs showed the highest conversion efficiency and improvement of 5.01 % on η as compared to that of reference platinum-based CEs.

CHAPTER ONE

INTRODUCTION

1.1 Background

Increasing energy prices and growing attention on global warming have motivated research on viable alternatives of energies to fossil fuels. Solar photovoltaic holds a great promise as the sun emits 120 000 Terawatts of radiation on the earth per year, which is the largest single source of clean energy (George & Nathan, 2007). Solar cell is an electrical device that converts light energy directly into electricity by photovoltaic effect, which is a physical and chemical phenomenon (Böer, 2002). Solar cells can be classified into first, second and third generation solar cells. As the first generation solar cells, silicon-based photovoltaic cells dominate the solar market due to their high efficiency of about 26.7 % (Green *et al.,* 2022). Silicon is naturally abundant and this has made silicon solar cells a popular choice since the p-n junction devices were fabricated in the 1950's (Chapin *et al.,* 1954). However, their indirect optical band gap requires a thick active layer for solar conversion, which results in the expensive fabrication of large area materials. This resulted to the invention of second generation photovoltaic (PV) materials to reduce the fabrication cost through the deposition of thin films (Brown & Kamat, 2008). The second generation cells are thin film solar cells, that include amorphous silicon, Cadmium telluride (CdTe) and copper indium gallium selenide (CIGS) cells. However, both first and second generation devices suffer the same performance restrictions, such as ''red losses'' (photons with energies below the band gap of the device cannot be absorbed) and ''blue losses'' (photons with energies above the band gap lose their excess energy as heat) (Wang *et al.,* 2011). Third generation photovoltaic, which represent the cutting edge of solar technologies, are designed to exceed the limits of single-junction devices for a high efficiency and a low production cost (wu *et al.,* 2008). The categories of third-generation solar cells include dye-sensitized solar cells (DSSCs), quantum dot-sensitized solar cells (QDSSCs), organic solar cells and hybrid Perovskite solar cells. These solar cells have a similar

structure consisting of a photoanode, counter electrode (CE) and a medium for charge transport. The working principle is also similar. Dye-sensitized solar cells (DSSCs) are currently the leading photovoltaic device with regards to third generation Photovoltaics (O'Regan and Grätzel, 1991). Since a prototype for DSSCs was reported by O'Regan and Gratzel, 1991, they have attracted a lot of intense interest (Ye *et al., 2015).*

A typical DSSC utilizes platinum on conducting glass as the counter electrode. The Pt is the most expensive component of a typical DSSC, making a cost of around 60–70 % of the total cost of DSSC (Arbab *et al.,* 2018; Sun *et al.,* 2018). Nevertheless, the extensively used Pt coated conducting glass produces an exceptional electro catalytic activity for reduction of triiodide ions at the CE, the cost and scarcity of the Pt limits the large-scale low-cost production of DSSC for commercial applications in future and thereby enabling the researchers to shift their focus on alternate materials to be used at the counter electrode to reduce the cost and improve on the conversion efficiency of the solar cells (Zhang *et al.,* 2018). In this work, Graphene incorporated on Pt based CEs is demonstrated to improve on the conversion efficiency and reduce the amount of Pt applied on DSSCs.

1.2 Statement of the Problem

The need for green energy has led to the need for more compliant materials. DSSCs are set to enter the market and thus there is need to address some of their pertinent problems. The power conversion efficiency of conventional DSSC is relatively low. Currently, a lot of research is directed towards increasing the conversion efficiency through structural modification of the solar cells using novel materials. The CE's which is the main component of DSSC reduces redox species which are used as mediators in the regeneration of the sensitizer after electron injection, determines the conversion efficiency (Gratzel, 2003). In this work, a novel material, graphene is incorporated in the traditional platinum-based counter electrode as a double-edged means of enhancing efficiency. Graphene with high conductivity and high transmittance will increase the

catalytic activity of Pt-based counter electrode and this will enhance the conversion efficiency of the solar cell.

1.3 Justification

The aspect of increasing efficiency in DSSCs calls for the modification of the cells using novel materials with excellent optoelectronic and mechanical properties such as graphene. Through introducing graphene in the counter electrode, the efficiency of the DSSC is improved due to enhanced catalytic activity. This is because of the electron tunneling aspect of Pt on Gr interface introduced to supplement the electrochemical process of the redox couple reduction. Graphene has a very high electrical conductivity, high transmittance, high charge mobility, exhibits ballistic transport and is ambipolar (Holes and electrons charge carriers can be alternated) and thus can easily transport the reactant species in DSSCs back to the Pt effectively and efficiently hence reducing the chances of electron-hole recombination in the DSSC dye (Dou *et al.*, 2012). The Pt film resting on graphene is maximally dispersed and stabilized by the high surface area graphene. In addition, graphene is mechanically and thermally stable, a property that makes it capable of operating under high temperatures.

1.3 Hypothesis

There is no relationship between electron-conduction and conversion efficiency on dye sensitized solar cells with different number of Pt on graphene layers as counter electrode.

1.4 Objectives

1.4.1 General Objective

To deposit platinum on different layers of graphene as counter electrode and apply to dye sensitized solar cell and evaluate the performance.

1.4.2 Specific Objectives

i. To synthesize and evaluate surface roughness and optical properties of titanium dioxide films, annealed at different rates, using optical microscopy and UV-VIS spectroscopy.
ii. To fabricate dye sensitized solar cells using working electrodes annealed at different rates and evaluate the I-V characteristics.
iii. To characterize the optical transmittance and sheet resistance of platinum on graphene layers counter electrode using UV-VIs spectroscopy and four point probe.
iv. To fabricate platinum/graphene layers and platinum counter electrode-based dye sensitized solar cells and determine the I-V characteristics.

CHAPTER TWO

LITERATURE REVIEW

2.1 Introduction

The aim of this chapter is to primarily discuss theoretical background of dye sensitized solar cells. A brief discussion on the structure, operational principle and characterization of DSSCs is given. The chapter also examines the unique and novel properties of graphene sheets and modifications of dye sensitized solar cells' structure with graphene sheets.

2.2 Structure of Dye Sensitized Solar Cells

Dye Sensitized Solar Cell (DSSC) utilizes the concept of excitonic injections and consists of a counter electrode substrate, a dye absorption titanium dioxide (TiO_2) and transparent photo-anode, as in figure in 2.1. A solution of iodine redox couples is used as the electrolyte in the cell (O'Regan & Grätzel, 1991). The modern DSSC cell has its roots from Michael Gratzel and Brian O'Regan in 1988 (O'Regan & Grätzel, 1991). Solar cell converts photon energy to electrical energy through imitating the natural photosynthesis process (Hemamali & Kumara, 2013).

The working electrode consists of a semiconductor attached to fluorine-doped tin oxide which is the conducting substrate (O'Regan & Grätzel, 1991). The sensitizing dye acts as the light absorbing layer and the electrolyte (redox system) contains the redox couple iodide/triiodide. The counter electrode is conventionally a platinized conducting substrate that transports holes away from the DSSC (O'Regan & Grätzel, 1991).

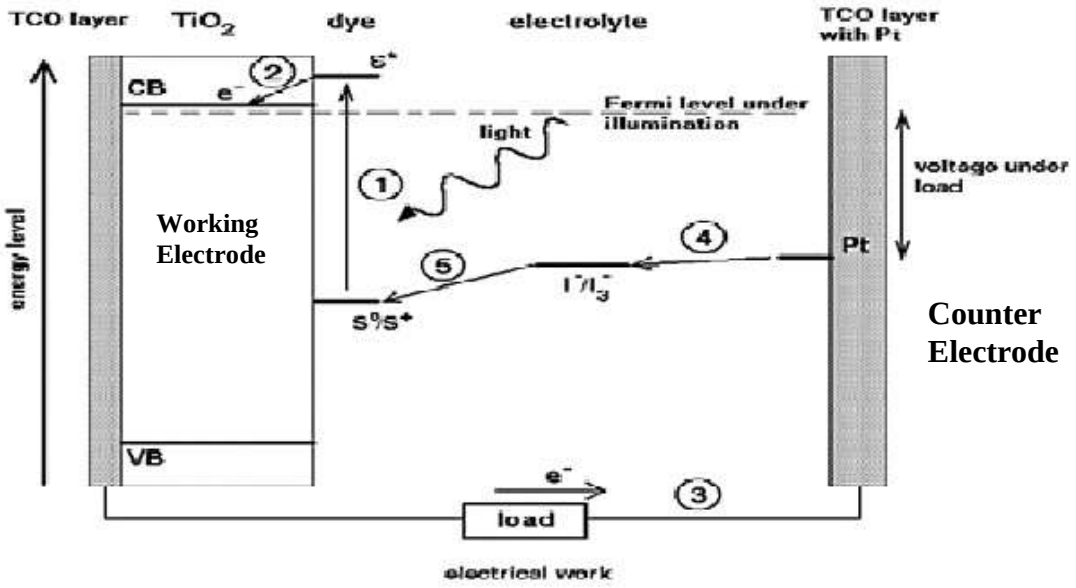

Figure 2.1: Structure of Dye Sensitized Solar Cell with Different Roles :(1) Photon Absorption,(2) Electron Injection,(3) Electrical Energy, (4,5) Redox Reaction

Source: (Chergui et al., 2010)

2.2.1 DSSC'S Counter Electrodes

The CEs moderate redox species in liquid solar cells, which are used as mediators in regeneration of the sensitizer after electron injection, or to accumulate holes from the hole conducting material in solid-state DSSCs (O'Regan & Grätzel, 1991). For an optimized cell, CE material should have lowest possible sheet resistance, excellent catalytic activity for the reduction of the redox electrolyte, high chemical stability and of low cost. The iodide–tri-iodide couple has been employed as the redox mediator and the overall redox reaction in DSSCs can be described as in equation 2.0 (Jasim, 2007).

$$I_3^- + 2e^- = 3I^- \quad \text{.....} \quad 2.0$$

Tri-iodide receives electrons from counter electrode and is reduced to iodide ions.

Platinum on conducting glass has been extensively employed as the standard CE for DSSCs due to its high catalytic activity and outstanding conductivity as well as its high corrosion stability alongside iodine as the electrolyte (Nazeeruddin *et al.,* 1997). However, the combination between the limited resource of platinum and the large application of platinum-based catalysts in the vehicle industry makes platinum extremely expensive and in diminishing supply. Therefore, it is important to explore Pt-free materials to replace the Pt counter electrode for DSSCs (Lim *et al.,* 2013). For this reason, recent attention has been focused on various materials as potential alternatives to Pt, including carbon (Grätzel *et al.,* 2003; Green, 2017) graphene, (Katumo *et al.,* 2015) transition metal sulfides, nitrides and carbides (Nam *et al.,* 2010).

2.2.2 Working Electrode of DSSC

It consists of transparent glass substrates which have high optical transparency in the visible and near infrared regions of the electromagnetic spectrum and a conducting film in the form of thin transparent conductive oxide (TCO) deposited on one side. The conductive film ensures a very low electric resistance per square units (Jasim, 2007). A nanostructured wide bandgap oxide semiconductor (electron acceptor) such as TiO_2 and ZnO_2 is grown on the conductive side to form the photoelectrode. The semiconductor gives high chemical stability of the cell due to their resistance to photo-corrosion. A layer of dye is adsorbed on the surface of nanostructured semiconductor to sensitize it for light absorption. The annealing rates and various structural changes of TiO_2 film affect the light-harvesting, charge-injection, and charge-collection properties of DSSCs, which, in turn, alter the photocurrent density, photovoltage, and solar energy conversion efficiency (Zhu *et al.,* 2007).

The energy gap value of TiO_2 depends on the films deposition conditions and its preparation method which influences in the crystalline structure (Pawar *et al.,* 2011).Variation in energy gap is due to variations in the structural and other properties of the deposited films. Band gap energy (E_g) of the TiO_2 films are obtained using the Tauc equation 2.1 (Pawar *et al.,* 2011; Tauc *et al.,* 1974).

$$(\alpha hv)^{\frac{1}{2}} = A(hv - E_g) \quad \text{..... 2.1}$$

Where, α = absorption coefficient, A = constant independent of photon energy and hv *(eV)* = energy of excitation.

2.2.3 DSSC Sensitizers

Dye molecules are used to sensitize the wide band gap of the photo electrode in the visible and infrared region of solar spectrum. The dye have a broad absorption spectrum, good stability and good marching of the high occupied molecular orbital (HOMO), lowest unoccupied molecular orbital (LUMO) levels of the dye with semiconductor's bottom edge of conduction band and chemical potential of redox system of electrolyte as in figure 2.2 (Mohammed *et al.,* 2015).

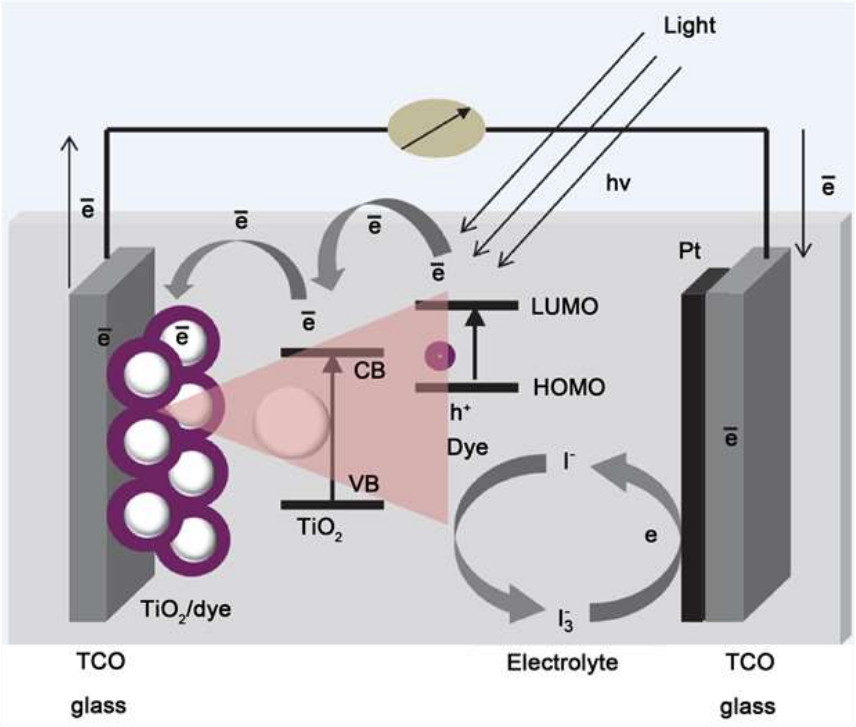

Figure 2.2: Schematic Diagram of Dye Sensitized Solar Cell under Light Illumination

Source: (Mohammed *et al.,* 2015)

In addition, chemical bonding between the dye and semiconductor's surface is necessary for effective electron transfer (Stathatos, 2008). Upon absorption of photon, a dye molecule adsorbed to the surface of nanostructured material gets oxidized and the excited electron is injected into the nanostructured material (Jasim, 2007). Commercially, there are five utilized sensitizers which include Ruthenium polypyidyl dye, porphyrin dyes, quantum dot sensitizer, metal free organic dyes, and Perovskite-based sensitizer. Ru (II) polypyridyl dyes exhibit excellent performance since they have a broad light absorption range from UV to near Infra-red with respect to TiO_2 photoanodes and I^-/I_3^-electrolyte. The dye also has a high molecular stability (Ye *et al.,* 2015).

2.2.4 Operational Principle of DSSC

Upon absorption of photons, dye molecules attached to the mesoporous TiO_2 surface absorbs photons of energy, *hv*, and dye molecules are excited from the HOMO to the LUMO states as given in equation 2.2 (Jasim, 2007).

$$TiO_2/S + hv \rightarrow TiO_2/S^* \quad \text{.....2.2}$$

Here, S is dye molecule and S* is the excited dye molecule.

Electrons in the LUMO of the dye will be transferred to the mesoporous TiO_2 within femtoseconds, ~10^{-15}s. This process is called electron injection (Jasim, 2007). The Fermi level of TiO_2 will be increased towards the conduction band (CB). Once an electron is injected into the conduction band of the wide bandgap semiconductor TiO_2 film, the dye molecule becomes oxidized as given in equation 2.3 (Jasim, 2007). The difference in the potential between the

Fermi and the redox levels will be manifested as the voltage of the device.

$$TiO_2 \,|S^* \rightarrow TiO_2\,|S^+ + e^-_{(CE)} \quad \text{..... 2.3}$$

The injected electron, $\mathbf{e}^-$, is transported from the conduction band of the TiO_2 and then transported to an external circuit as an electrical energy as given in equation 2.4 (Jasim, 2007).

$$e^-_{TiO_2} + C.E \rightarrow TiO_2 + e^-_{(CE)} + electrical\ energy \quad \text{.....2.4}$$

Electrolytes containing I^-/I_3^- redox ions are used as an electron mediator between the TiO_2 photo electrode and the counter electrode. Therefore, the oxidized dye molecules (photosensitizer) are restored by receiving electrons from the I^-ion redox mediator that get oxidized to I_3^-(Tri-iodide ions). This process is represented by equation 2.5 (Jasim, 2007).

$$S^+ + \tfrac{3}{2}I^- \rightarrow S + \tfrac{1}{2}I_3^- \quad \text{.....2.5}$$

In equation 2.6, S^+ is oxidized dye molecule and S is a dye molecule.

The I_3^-substitutes the internally donated electron with that from the external load and reduced back to I^- ion as illustrated in equation 2.6 (Jasim, 2007).

$$\tfrac{1}{2}I_3^- + e^-_{(CE)} \rightarrow \tfrac{3}{2}I^- + C.E \quad \text{.....2.6}$$

2.2.5 DSSC Characterization

The performance of a solar cell is mostly commonly characterized by three parameters, that include overall solar energy-to-electrical energy conversion efficiency (η, 'efficiency') under sunlight illumination, fill factor (FF), and the wavelength-dependent incident photon to current conversion efficiency (*IPCE*) (Neuthe, 2014).

These parameters can be calculated from the short circuit current density, $J_{SC,}$ and the open circuit potential, $V_{OC,}$ of the device, which are measured under sunlight illumination. A sample J/V curve, from which J_{SC} and V_{OC} are deducted, is given in figure 2.2 (Neuthe, 2014).

The short circuit current density is the maximum current output of the cell and measured at the point where the net voltage is zero. Its height is determined by the efficiency of the electron injection into the conducting band of the semiconductor and the collection efficiency at the photoanode. Similarly, the open circuit potential is the maximum voltage available from the cell measured at the point where the net current is zero (Neuthe, 2014). It is defined by the potential difference between the Fermi level in the semiconductor and the redox potential of the redox mediator. The product of J_{SC} and V_{OC} defines the theoretically possible maximum power P_{max} of a cell. The actual maximum power P_{max} of the cell is the product of photovoltage V_{MP} and photocurrent J_{MP} at the voltage where the power output is maximal as shown in figure 2.3 (Neuthe, 2014).

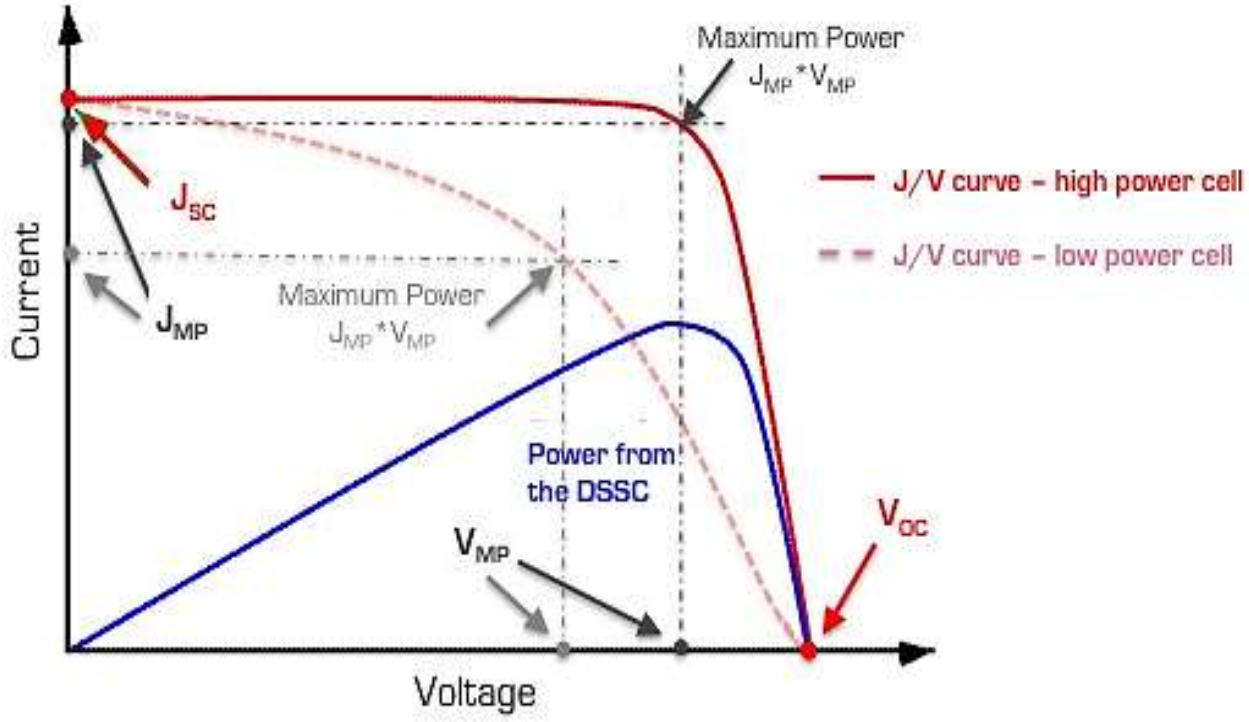

Figure 2.3: Current-Voltage Curve of a DSSC

Source: (Neuthe, 2014).

The Fill Factor (FF) measures the quality of the solar cell. This is calculated by comparing the maximum power to the theoretical power (P_T) that would be output at both the open circuit voltage and short circuit current together as given in equation 2.7. FF can also be interpreted graphically as the ratio of the rectangular areas (Stathatos, 2012).

$$FF = \frac{P\,max}{Voc \times Jsc} \quad \text{…..……..…. 2.7}$$

Where P_{max} is the maximum power of the solar cell.

Efficiency is the ratio of the electrical power output P_{out}, compared to the solar power input, P_{in}, into the PV cell as given in equation 2.8 (Stathatos, 2012).

$$\eta = \frac{P_{max}}{E \times A_C} \quad \text{.....2.8}$$

The third measure, the IPCE, expresses the external quantum efficiency. This is the external photocurrent density measured in the external circuit of the cell under monochromatic illumination at different wavelengths divided by the incoming photon flux (ϕ). The IPCE can be calculated as described in equation 2.9

$$IPCE\ (\lambda) = \frac{J_{SC}(\lambda)}{e\phi\lambda} = \frac{J_{SC}(\lambda)[Acm^{-2}]}{\lambda[nm]P_{in}(\lambda)[Wcm^{-2}]} \quad \text{.....2.9}$$

Where e as the elementary charge and λ is the wavelength.

2.3 Modification of Dye Sensitized Solar Cell using Graphene

Graphene is one-atomic layer of graphite which exhibits a two-dimensional honeycomb like carbon network (Li and Zhang, 2013). Graphene is the first truly 2D material ever observed in nature. Its discovery in 2004 ended the Mermin-Wagner theorem which states that 2D crystal loses its long-range order (stability), thus melts due to thermal fluctuations in the lattice (Enoki & Ando, 2013). It was first synthesized in 2004 by Andre Geim and Konstantin Novoselov (Novoselov *et al., 2004*). It is mostly produced from highly ordered pyrolytic graphite (HOPG) through mechanical exfoliation process (Novoselov *et al.,* 2004), epitaxial growth on silicon carbide and chemical vapor deposition (CVD) (Dodo-Arhin *et al.,* 2013; Matte *et al.,* 2011). It has a linear dispersion relation near the *K* and *K'* points which makes it a gapless semiconductor (Novoselov *et al., 2004*).

2.3.1 Crystal Structure of Graphene

Graphene has carbon-carbon bonds that are very strong. These bonds give graphene its extraordinary mechanical strength and flexibility in the atomic scale. The structural flexibility of graphene is reflected in its electronic properties. It has a young's modulus of 2.4 $\pm$ 0.4 TPa, making it the stiffest material known currently in atomic scale (Lee *et*

al., 2012). The flexibility aspect of graphene is reflected in its electronic properties through hybridization. The electronic structure of an isolated carbon atom is [He] $(2s)^2$ $(2p)^2$. The [He] electrons remain inert while the 2s and 2p overlap to form hybrid bonding orbitals (Choi & Lee, 2011). Unlike diamond which is formed through formation of four sp^3 orbitals, establishing the tetrahedral bonding that soaks up all valence electrons, graphene is formed from three sp^2 orbitals which arrange themselves in a plane at 120^O angles. This forms the honeycomb lattice of graphene (Choi & Lee, 2011). Of the sp^2 hybridized carbon atoms, three of the valence electrons 2S, P_x and P_y form sigma bonds (σ-bonds) with their next neighbors. The orbital of the fourth electron, referred to as π- electron, is oriented perpendicular to the plane forming a network of delocalized π-bonds. These are the bonds which lead to the formation of the planar layer with a honey-comb-like structure (Choi and Lee, 2011). The σ is responsible for the robustness of the lattice structure in allotropes. As a result of Pauli Exclusion Principle, these bands have a filled shell and thus form a deep valence band (Neto *et al.*, 2009). The unaffected *p* orbital, which is usually perpendicular to the planar structure, binds covalently with the neighboring atoms forming the π band as shown in figure 2.4. The π band is usually half filled because each *p* orbital has one extra electron (Neto *et al.*, 2009).

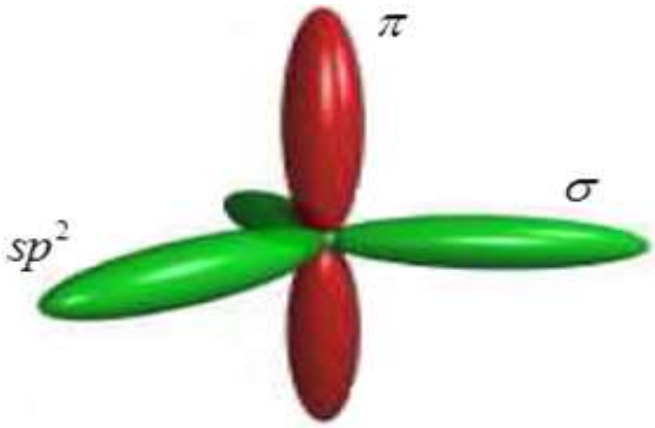

Figure 2.4: Schematic Diagram of Electron Σ And Π Orbitals of One Carbon Atom in Graphene

Figure 2.5 shows the idealized 2D graphene which forms a honeycomb lattice (Guo *et al.*, 2009).

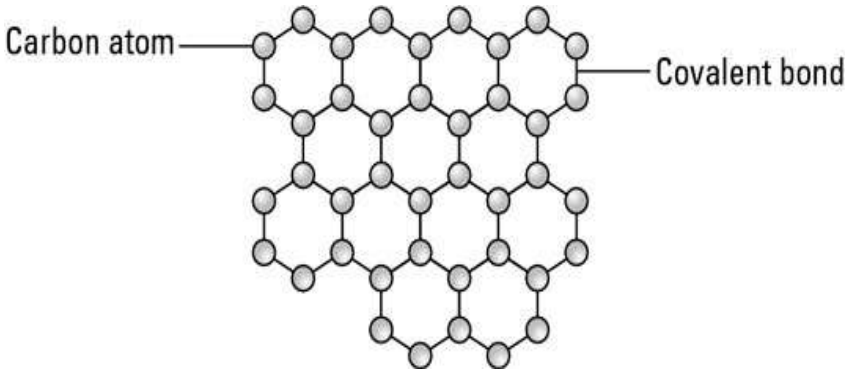

Figure 2.5: Idealized Crystal Structure of a Single Graphene Sheet

The Dirac points in the Brillouin zone (K= 0) which presents the dispersion relation of graphene in 3D view is as indicated in figure 2.5. The inverted cones on the upper side represent the conduction band while the lower ones indicate the valence band. These cones which touch at the peaks as indicated in the enlarged part of figure 2.6 indicate that graphene is a zero-band-gap semiconductor.

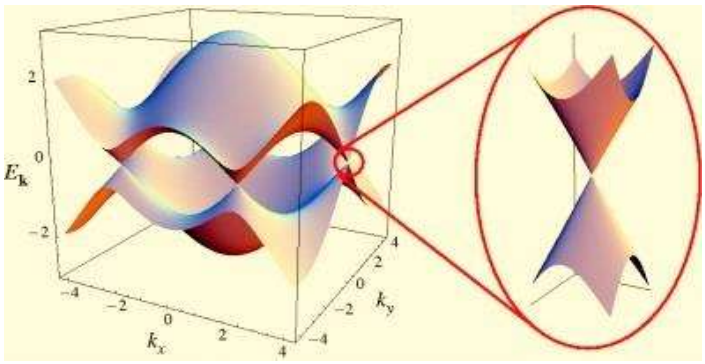

Figure 2.6: Graphene's electronic band dispersion in the honeycomb lattice

Source: (Neto *et al.*,2009).

The K and K' points are the corners of the hexagonal Brillouin zone. This enables the conduction of electrons in graphene behave as massless Dirac fermions (Enoki & Ando, 2013). This phenomenon makes graphene have unique electron transfer properties.

2.3.2 Properties of Graphene

The crystal structure is dictated by its geometry and number of layers. Graphene exhibits amazing optical, electronic, thermal and mechanical properties and hence it is a promising material for technological advancement in DSSCs and other technologies such as surface enhanced spectroscopy, photo-detectors and frequency analog ballistic transistors (Das *et al.*, 2014). Its excellent properties make it a promising material for development of TCOs in DSSCs (Novoselov *et al.*, 2004). The material is mechanically hard, chemically inert, thermally stable, and exhibits 97.7% transmittance throughout the entire visible spectrum (Novoselov *et al.*, 2004; Das *et al.*, 2014). The electronic band structure of graphene experiences a linear dispersion property at the Fermi Level (E_f) with gapless excitations hence making it behave as massless Dirac fermions (Das *et al.*, 2014). Graphene has a carrier mobility of 2.6×10^5 cm^2 V^{-1} s^{-1} (Jayawardena *et al.*, 2013).

Monolayer graphene can absorb ~2.3 % of light. This value can be defined solely by $\pi\alpha$ based on the Dirac cone approximation, which is only valid for the coupling between light and relativistic electrons near the Dirac point (Nair *et al.*, 2008).

Multilayer graphene is a graphene thin film with weak van der Waals interaction between the layers, and its electronic and optical properties are sensitive to the number of layers as well as the stacking sequence (Neto *et al.*, 2009; Mikhail, 2012). A fast and reliable method to determine the layer number is desired in the can be determined using transmittance at normal incidence 550 nm with the application of equation 2.10 (Avouris, 2010).

$$T = [1 + 1.13\pi\alpha\frac{N}{2}]^{-2} \quad \text{.....2.10}$$

Where T is the transmittance, α is fine structure constant and *N* is the number of graphene layers

2.3.3 Applications of Graphene

The novel properties of graphene make it a promising material for optoelectronic circuits such as field effect transistors, transparent optoelectronics, biological sensors, heat spreaders, transparent conducting electrodes (TCEs), flexible optoelectronics, photo-detectors and energy harvesting devices (Novoselov *et al.,* 2004; Lemme, 2010; Das *et al.,* 2014). Further graphene has also been used for energy storage, electrochemical device and high-speed switching devices (Li & Zhang, 2013; Raccichini *et al.,* 2015). The unique electronic and optical properties make graphene a suitable alternative counter electrode in DSSCs.

2.3.4. Graphene Based Dye Sensitized Solar Cells

Platinum-loaded conducting glass has been widely employed as the standard CE for DSSCs due to its high catalytic activity and excellent conductivity as well as its high corrosion stability against iodine in the electrolyte (Kim *et al.,* 2006). However, the combination between the limited resource of platinum and the large application of platinum- based catalysts in the vehicle industry makes platinum extremely expensive and in diminishing supply. Therefore, it is important to explore Pt-free materials to replace the Pt counter electrode for DSSCs (Olsen *et al.,* 2000). Current research in DSSCs is focused on identifying appropriate materials as alternative to critically important materials such as platinum and indium in the fabrication. Carbonaceous materials are proving to be excellent alternative materials. Multi-walled carbon nanotubes (MWCNTs), double-walled carbon nanotubes (DWCNTS) and single-walled carbon nanotubes (SWCNTs), graphene nanosheets (GNs) have all indicated functionality and high conversion efficiencies when utilized as counter electrodes in DSSCs (Zhang, 2011). Currently, the main drawback of carbon-based counter electrodes is the requirement of a large amount of carbon to reach comparable

efficiencies to Pt-based CEs. This makes the device bulkier and more opaque (Murakami and Graetzel, 2008). As a rising star in the carbon family, graphene, with its unique properties, is being explored as a DSSC counter electrode to solve these issues. Graphene based materials are receiving attention as photoanodes, photosensitizers and counter electrodes in DSSCs (Singh & Hari, 2015). Graphene has been used as photoanode and photoanode composite in DSSCs (Kim *et al.*, 2015)

CHAPTER THREE

MATERIALS AND METHODS

3.1 Introduction

Preparation and characterization of TiO_2 films on FTO using optical microscopy and UV-VIS spectrophotometer is described. It also explains preparation and characterization of platinum and platinum on graphene CEs using UV-VIS spectrophotometer. Specifically the transmittance and sheet resistance of graphene based CE is evaluated. Finally, the procedure for I-V characterization of DSSCs is discussed.

3.2 Preparation of TiO_2 as a Working Electrode

The WE is the TiO_2 semiconducting film deposited on FTO substrate where the dye that absorbs photons is adsorbed on it (O'Regan & Grätzel, 1991). The preparation of TiO_2 involved cleaning, doctor blading, annealing and sintering of TiO_2 films.

3.2.1 Cleaning

In cleaning FTO (SnO_2: F) glass substrates (Melting point <1000 ^{0}C, *Xinyan* Technology Co. Limited, China) the method used by Mohamd *et al* 2015 was adopted. The FTO glass was cut into 1.5 x 2 cm pieces using the diamond cutter. Glass substrates and the tempered glass were then cleaned for five minutes in acetone (purity 99.5%) using cotton swabs. The substrates were then transferred into ethanol (purity 99.5%) and cleaned for five minutes then rinsed with deionized (DI) water for five minutes. they were then dried with warm pressurized air and kept in clean samples boxes.

3.2.2 Application of Titanium Nanoxide Paste through the Doctor Blade Procedure

The TiO_2 films as working electrode was synthesized by a doctor-blade method which was described by previous researchers (Koo *et al.*, 2008).

A 1 x 1 cm^2 window was cut from a scotch tape and placed on the conductive side of the FTO glass substrates. The titanium nanoxide T/SP (18 % wt, 15-20 nm, *Solaronix*, Switzerland) was stirred manually using a clean glass rod. Titanium nanoxide paste was doctor bladed on the conductive side of the FTO substrates using the cleaned tempered glass. The scotch tape was removed carefully and the coated glass was then covered by Petri dish for 30 minutes to dry and also enhance homogeneity. The thicknesses of the films that were established to be 0.3 μm using Nanovea-PS50 optical profilometer were controlled through applying uniform pressure in the pasting region.

3.2.3 Drying and Sintering

Different annealing rate processes were evaluated to affect the performance of platinum based DSSCs which acted as reference cell for the platinum on graphene and graphene DSSCs. The prepared TiO_2 samples were kept in a dark box for 20 minutes to enhance homogeneity (Benjamin *et al.,* 2018). The samples were then subjected to the different annealing rates. The annealing rates were 1 ^{O}C/minute, 2 ^{O}C/minute, one step annealing at 450 ^{O}C and as deposited samples. In the first annealing process, the annealing rate was set at 1 ^{O}C/minute and the photoanodes were sintered at 450 ^{O}C for 30 minutes in a KL20 furnace. They were let to cool in the furnace. These working electrodes were named WE-A. The second process of annealing involved a 2 ^{O}C/minute annealing rate up to 175 ^{O}C and subsequent sintering for 30 minutes at 450 ^{O}C. These WEs were labeled WE-B. In the third annealing process, WEs were subjected to sintering at 450 ^{O}C for 30 minutes and WE labeled as WE-C. In the fourth annealing process, the WE were left to dry at ambient temperature of 27 ^{O}C for 2 hours and WEs labeled WE-D.

3.3 Preparation of Platinum Counter Electrode

3.3.1 Cleaning

Prior to use, the FTO glass substrates (2.0 x 1.5 cm, sheet resistance of seven ohms per square, 7 Ω/sq) and the tempered glass were cleaned using acetone (purity 99.5%),

ethanol (purity 99.5%) and DI water sequentially for five minutes in each step. The glass substrates were then dried using pressurized warm air (Katumo *et al.,* 2015)

3.3.2 Applying Platisol T/SP

A scotch tape was cut into 1 x 1 cm^2 window and placed on the conductive side of the FTO glass substrates. A thin layer of Platisol T/SP (*Solaronix,* Switzerland) was doctor bladed on the conductive side (Koo *et al.,* 2008). The films were then kept for 20 minutes in a clean dark box to enhance homogeneity after which they were heat treated at optimized annealing rate of 2 ^{O}C/min and sintered at 400 ^{O}C for 30 minutes to activate the Pt film (Cheng *et al.,* 2016). They were let to cool in the furnace after which they were used to fabricate the DSSCs. The transmittance of the samples was obtained using Shimadzu SolidSpec-3700DUV spectrophotometer.

3.4 Preparation of Platinum/Graphene Counter Electrodes

3.4.1 Cleaning

The graphene coated FTO SnO_2: F glass substrates (1.5 x 2 cm), (*Graphene Laboratories Inc*., USA) were soaked in ethanol for five minutes and then thoroughly rinsed with DI water for 5 minutes. The films were then dried using pressurized air and placed in a hot air furnace 50 ^{O}C for 30 min to dry where they were retrieved for coating (Katumo *et al.,* 2015).

3.4.2 Applying Platisol T/SP

A scotch tape was cut into 1 x 1 cm^2 window and placed on the conductive side of the graphene coated FTO glass substrates. A thin layer of platisol T/SP (*Solaronix*, Switzerland) was doctor bladed on the graphene side. The films were then kept for 20 minutes in a clean dark box to enhance homogeneity after which they were heat treated at an annealing rate of 2 ^{O}C/minute and sintered at 400 ^{O}C for 30 minutes to activate the Pt on graphene film (Katumo *et al.,* 2015). They were let to cool in the furnace after

which were used to fabricate the DSSCs. Prepared CEs were analyzed using Shimadzu SolidSpec-3700DUV spectrophotometer. The Pt film thickness was measured to be 0.1 µm using Nanovea-PS50 optical profilometer.

3.5 Preparation of Electrolyte Solution

Iodine electrolytes (0.1 mM) solution was prepared through adding lithium iodide (LiI) to 100 ml of acetonitrile while stirring. Then 1.3 g of iodide added to the solution while stirring continuously (Wu *et al.,* 2008).

3.6 Preparation of Ruthenium Dye

In preparation of the ruthenium dye, the methods that were earlier reported were adopted (Nazeeruddin *et al.,* 1997; Katumo *et al.,* 2015). A 0.5 mM cis-diisothiocyanato-bis (2,2'-bipyridyl-4,4'-dicarboxylato) ruthenium (II) bis (tetrabutylammonium), (N719 dye) was prepared through dissolving 200 mg of the N719 dye (Solaronix, Switzerland) in 100 ml of ethanol (purity, 99.5 %) in a conical flask and stirred for the dye to dissolve. This was then followed by addition of 236.53 ml of the ethanol. The conical flask was then sealed and then rotated for 10 minutes using a digital shaking rotator for N719 dye to dissolve. The 0.5 mM concentration of dye is recommended for better dye adsorption on the WEs (Katumo *et al.,* 2015). The solution was then kept in a dark room ready for use. The preparation of the 0.5 mM N719 dye was in accordance to the equation 3.1 (IUPAC, 1997)

$$c = \frac{m}{v} \times \frac{1}{mw} \quad \text{..... 3.1}$$

Where, *C* is the molar concentration in mol/L, m is the mass of the N719 in grams, V is the formula weight, the sum of the atomic weights of the atoms in a substance's chemical formula, and MW is the molar weight, mass of molecules of substance, of the N719 dye, which is 1188.6 g/mol. The molecular formula of N719 dye is $C_{58}H_{86}O_8N_8S_2Ru$ (Ryan, 2009).

3.7 Assembly of DSSC

DSSC was assembled using the procedure that was earlier reported (Kang *et al.*, 2015; Sultana *et al.*, 2023). Dye-coated TiO_2 electrode was sealed with the platinum-coated FTO counter electrode using a dupont surlyln (meltonix 1170-25 solaronix) a thermal plastic hot-melt sealant with a thickness of 50 µm leaving a small space for the electrolyte introduction. The electrolyte was then introduced into the space between the electrodes then sealed at 70 ^{O}C. The solar cell was then characterized by analyzing the I-V characteristics obtained through applying an external bias on the cell in a dark room. A 450 W halogen lamp adjusted to an intensity of 100mW/cm^2 was used. The irradiance on the DSSC's was maintained at 1 sun, 100 mW/cm^2 with the use of a solar power meter TM206 and single crystal Si photoanode. During characterization, the cells were covered with a black-printed paper with a hole measuring 1cm^2 for the active area. The following parameters were taken; open circuit voltage, short circuit current, and FF. The FF and conversion efficiency were calculated from I-V curve using equation 2.7 and 2.8 respectively. A model of the preparation of the DSSCs is illustrated in figure 3.1.

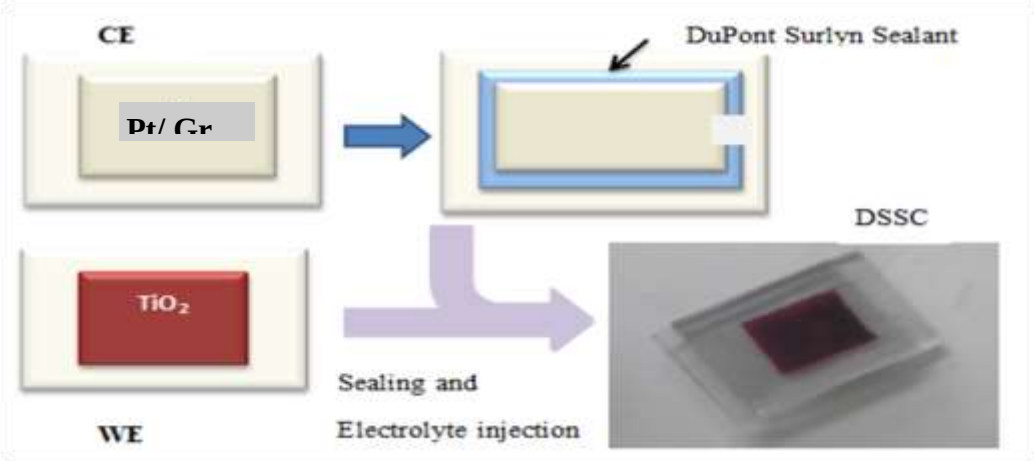

Figure 3.1: Schematic Representation of Fabricated DSSC

Source: (Katumo et al., 2015).

3.8 Characterization of WEs and CEs

3.8.1 Optical Microscopy of TiO_2 Thin Films

An optical microscope, Zeiss Axio Zoom V16, in reflection mode was used to obtain optical images of the films at magnifications 16 X, 100 X and 260 X. The incident light ($400 \leq \lambda \leq 800$nm) emitted by LEDs mounted on the sides of the stage of the microscope was reflected by the TiO_2 films, passed through a 1mm aperture into the lens and finally by an AxioCam Mrc5 high resolution charge-coupled device (CCD) camera (pixel size: 3.4×3.4 μm) interfaced with a computer. The CCD was used to acquire 8-bit images at 2584×1936 (5 Mpixel) resolution. 3D optical images of different TiO_2 thin films were then analyzed using *imagej 1.48v* software.

3.8.2 Transmittance of TiO_2 Thin Films

The Shimadzu SolidSpec-3700DUV spectrophotometer, spectrum bandwidth 5 nm and wavelength range of 340 – 1000 nm was used to record the transmittance of the various working electrodes and counter electrodes. For transmission, the single beam configuration for transmission was used with blank FTO being the reference. Figure 3.2 shows the transmission model of the SolidSpec 3700DUV UV-VIS-NIR spectrophotometer (Corporation S, 2015). After the baseline was set, the working electrodes were placed in the sample compartment cell and then spectra were displayed in the display window. Data points were then taken for each sample and analyzed using *origin pro* 8.6 version.

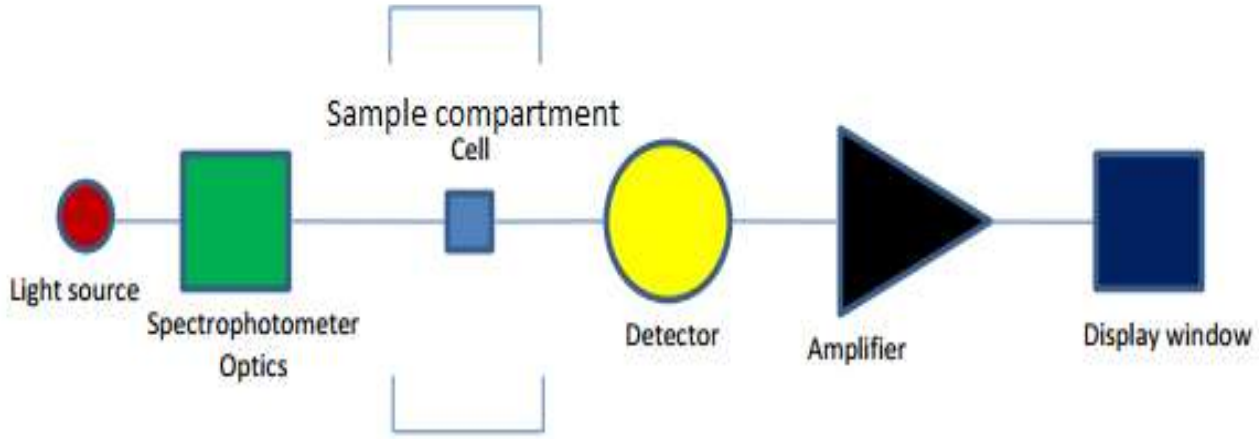

Figure 3.2: Basic Layout of a Single Beam Transmission of SolidSpec 3700DUV Spectrophotometer

Source: (Corporation S, 2015).

3.8.3 Sheet Resistance of Graphene CEs using Four Points Probes

This was done through contacting four equally-spaced (1 × 1 inch) co-linear probes to surface of graphene CEs. Figure 3.3 is schematic diagram of four-point probe (OH. C, 2005; Smits, 1958)

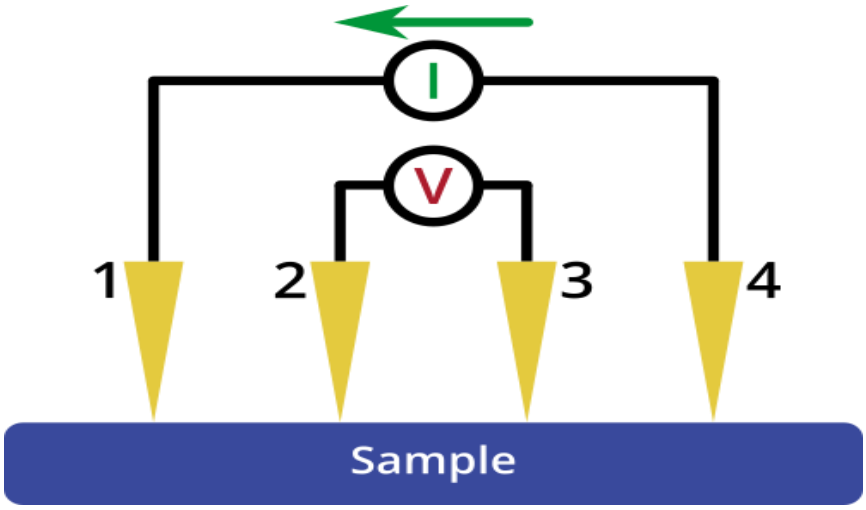

Figure 3.3: Schematic Diagram of Four-Point Probe Circuit

Source: (OH C, 2005).

A DC current was applied between the outer two probes (1 and 4) and a voltage drop measured between the inner two probes (2 and 3). The sheet resistance of CEs then calculated using the equation 3.2 (Smits, 1958).

$$R_S = \frac{\pi}{\ln(2)} \frac{\Delta V}{I} = 4.53236 \frac{\Delta V}{I} \quad \text{.....3.2}$$

Where, R_s is the sheet resistance, ΔV is the change in voltage measured between the inner probes, and I is the current applied between the outer probes (OH C, 2005; Smits, 1958).

CHAPTER FOUR

RESULTS AND DISCUSSIONS

4.1 Introduction

In this chapter, results are presented and discussed with the aid of images, graphs and tables. This chapter begins with the results of effect of annealing rates on the surface roughness, transmittance, band gap energy and electrical property of TiO_2 thin films on FTO. Results of transmittance of Gr and platinum on graphene layers CEs are also presented, analyzed and discussed. Electrocatalytic of platinum-based counter electrode using graphene layers is analyzed and discussed.

4.2 Optimizing Annealing Rates of Working Electrodes

4.2.1 Surface Roughness of TiO_2 Thin Films

Surface roughness of TiO_2 treated under different thermal conditions was evaluated by studying the 2D microscopic images. Figure 4.1 shows 2D optical image of TiO_2 deposited on FTO obtained at magnification of 260 X. The variations in contrast regions indicate variations in surface topographies of films, which become clearer at high magnification. Thin films annealed at 1 ^{O}C/min and 2 ^{O}C/min was relatively uniform and had minimal cracks unlike one step annealed samples.

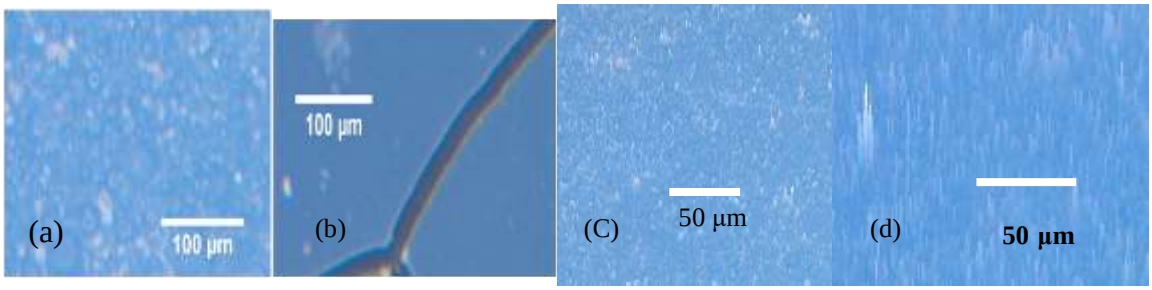

Figure 4.1: TiO2 Films Deposited on FTO Glass Annealed at (a) as Deposited, (b) One Step (c) 2 OC/min and (d) 1 OC/min Obtained at 260 X Magnifications.

The surface roughness of 3D images of TiO_2 thin films was analyzed by plotting line profiles at four different positions of 50 μm on the image spanning the whole area and average topographical heights recorded, using *imagej 1.48V* software, as shown in figure 4.2. In order to ensure reproducibility, the procedure was repeated on three other samples which had been prepared under similar conditions. From figure 4.2, the topographical heights were noted to change with distance on the images.

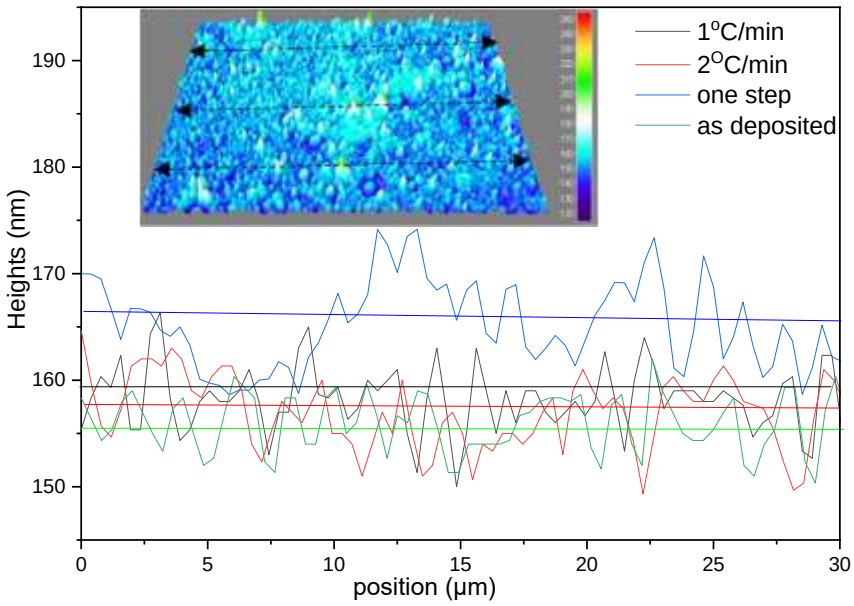

Figure 4.2: Topographical Heights as a Function of Position Obtained by Use of Image j 1.48 (Inset- 3D Image with Lines Where Profiles Were Obtained)

The plots depicted regions of high elevations (peaks) and lower elevation (valleys) from mean heights. As can be seen variation in topographical heights is highly dependent on surface roughness, with 1 ^{O}C/min samples showing a lower variation of 0.1568 μm and one step annealed samples being the highest with 0.1676 μm is shown in figure 4.3.

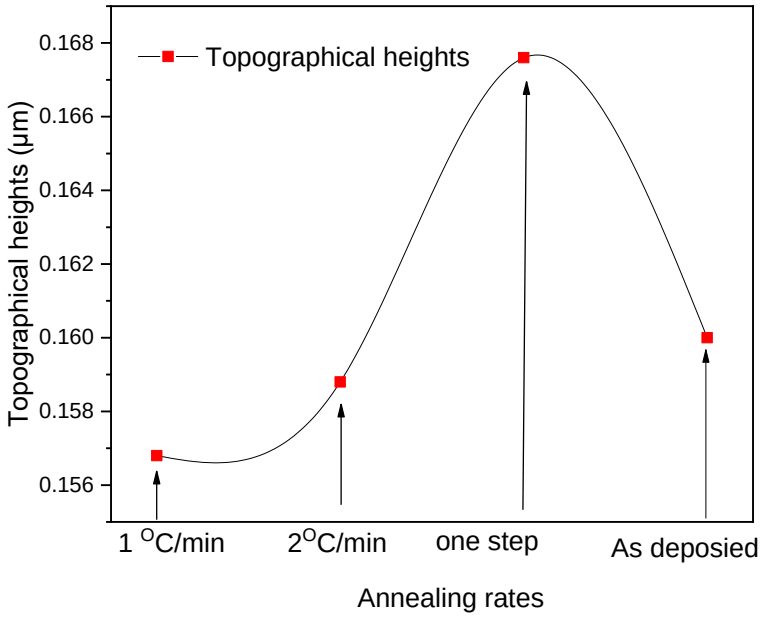

Figure 4.3: Variation of Topographical Heights with Annealing Rates

With lowering of annealing rates the surface topographical heights reduces as summarized in table 4.1. The low topographical heights depict improved surface roughness. Thin films given one step annealing at 450 ^{O}C for 30 min, are characterized by defects such as cracks and agglomerations, thus showing a higher variation in topographical heights depicting a high surface roughness. Areas with cracks are characterized by low topographical heights and those with agglomeration with high topographical heights.

Table 4.1: Variation of Topographical Heights with Annealing Rates

Annealing rates	**Topographical heights (µm)**		
	Minimum	**Maximum**	**Average**
1^{O}C/min	0.1545	0.1591	0.1568 ± 0.00231
2^{O}C/min	0.1535	0.1641	0.1588 ± 0.0053
One step	0.1501	0.1750	0.1676 ± 0.01245
As deposited	0.1642	0.1654	0.1600 ± 0.0006

The variation in roughness is attributed to the growth of small globules of TiO_2 with some areas agglomerated on the glass substrate (Benjamin *et al.,* 2018). Lowering of annealing rate, 1 ^{O}C/min and 2 ^{O}C/min, the surface roughness reduces and become more homogeneous, causing more growth of TiO_2 particles on the substrate and less agglomeration. The high surface roughness on one-step annealed films is attributed to the film being mainly amorphous and thus begins to crystallize into anatase phase after annealing at 400 ^{O}C (Naceur *et al.,* 2012). Low annealing rate enhances both the mobility of molecules as the particle crystallization simultaneously takes place (Tian *et al.,* 2006). The enhanced mobility of molecules makes the surface of TiO_2 smooth and cracks free, that is, crystallization granulates the surface. Thus, the mobility of molecules played a primary role in the change of morphology (as observed in the 1 ^{O}C/min and 2 ^{O}C/min annealing rates) and as a result, the surface roughness decreased as the films became more homogeneous. Low annealing rates gives the atoms activation energy for them to nucleate hence improving the film quality which results to a decrease in grain boundaries and less cracks (Wibowo *et al.,* 2017; Muaz *et al.,* 2016). The as deposited films have high topographical heights due to lack of thermal treatment to evaporate the organic solvents in the TiO_2 paste.

4.2.2 Optical Properties of TiO_2 Thin Films

The transmittance spectra were obtained using UV-Visible spectrophotometer in the range of 280-800 nm. From figure 4.4, it can be observed that the transmittance of the TiO_2 thin film increases with increase in wavelength which can be attributed to low absorbance of TiO_2 at longer wavelength (Perdana & Dahlan, 2013; Listanti *et al.,* 2018). These curves show the influence of annealing rates on the optical properties of titanium dioxide thin films. In general, the shape of the transmittance spectra is almost identical and these spectra consist essentially of two parts: A region characterized by a strong absorption located at $\lambda < 400$ nm which is practically in the Ultra Violet field and is mainly due to the electronic inter-band transition (Zhang *et al.,* 2004). It also comprises of a region of high transmittance which is in visible range, 400 to 800 nm, and is in the order of 80 to 90 % for all the films. This high transmittance is one of the

essential characteristics that justify the interest in TiO_2 thin films. They show that titanium dioxide thin films are transparent in the visible and opaque in the ultraviolet (Zhang *et al.,* 2004). Lowering of annealing rates leads to a small fluctuation band shift towards lower wavelength that can be attributed to nanoparticles increase in number and size. Low annealing rates, (1 ^{O}C/min), increase film homogeneity, with improvement of surface roughness promoting the increase of the surface scattering of the light by increasing the columnar growth with needle and rode like shape which as a result lowers the transmittance of the films (Hassan *et al.,* 2008; Zhang *et al.,* 2004). At the visible regions absorption decreases and at high wavelength the incident photons have no enough ability (energy) to make interaction with materials so photons will be transmitted, when wavelength decreases (photon energy increase) the photons are absorbed. The interaction between incident photons and TiO_2 leads to increase in the absorbance as deduced from the results (Stereeman, 1980).

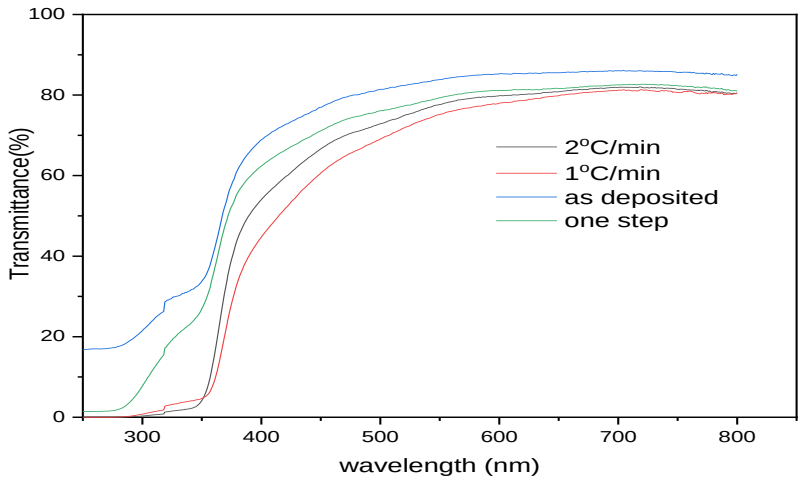

Figure 4.4: UV-VIS Transmittance Spectra of TiO2 Thin Films Deposited on FTO Annealed at Different Rates

Band gap energy (E_g) of the films annealed at different rates was obtained using the Tauc plot. (Pawar *et al.,* 2011; Tauc *et al.,* 1974). The value of E_g is obtained by

extrapolating the straight-line portion of the plot to zero absorption edge in graph of $(\alpha hv)^{\frac{1}{2}}$ versus energy axes (hv), the evaluated E_g of TiO_2 thin film is shown in figure 4.5.

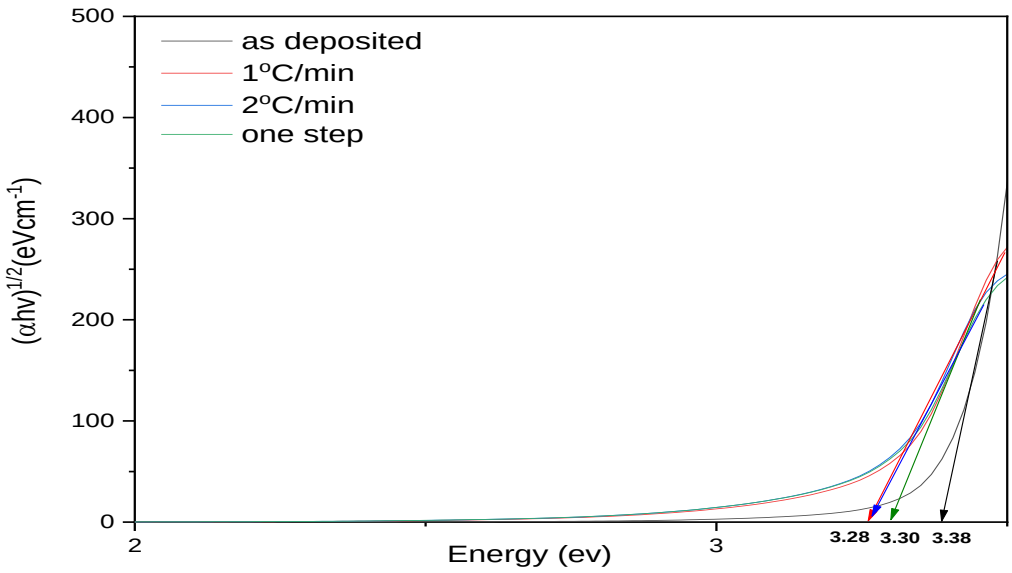

Figure 4.5: Tauc Plot for Indirect Transition for TiO2 Thin Films Annealed at Different Rates.

The values of E_g are found to be 3.38, 3.30, 3.28 and 3.28 *eV* for the films annealed at; as deposited, one step, 1 ^{O}C/min and 2 ^{O}C/min respectively. As deposited TiO_2 thin film has the highest energy band gap of 3.38 *eV* and the thin films annealed at 2 ^{O}C/min and 1 ^{O}C/min have slightly lower value of 3.28 *eV*. The band gap is observed to reduce with lowering of annealing rates with 1 ^{O}C/min and 2 ^{O}C/min having the lowest. The process of annealing affects the material by improving crystallinity and surface roughness that led to decrease in the value of E_g and this may be due to quantum confinement. Annealing of TiO_2 thin films leads to increased levels of localized near valence band and these levels are ready to receive electrons and generate tails in the optical energy gap and tail reduce the E_g, or can be attributed to increase crystals sizes in the films

(Tipparach *et al.,* 2008). Sankar *et al* also made a similar observation that E_g of TiO_2 reduces when annealed (Sankar *et al.,* 2009).

4.2.3 I-V Characteristics of DSSC's Fabricated from TiO_2 WEs Annealed at Different Rates

Platinum was used as the standard counter electrode in these solar cells. Working electrode left to dry at ambient temperature (as deposited) were investigated and shown to produce very low performance as compared to annealed samples. TiO_2 annealed at 450 ^{O}C for 30 min (one step) were found to give low performance compared to the ones annealed at 1 ^{O}C/min which produced the best performance of 3.31 %. Working electrodes annealed at 2 ^{O}C/min were also found to give high conversion efficiency of 3.11 %, as summarized in table 4.2. FF and η of the fabricated DSSCs were calculated using equation 2.7 and 2.8, respectively.

Table 4.2: Photovoltaic Performance of the Different Platinum CE Based DSSCs with WEs Dried and Sintered at Different Rates

Sample	V_{OC} (v)	J_{SC} (mA/cm^2)	F.F (%)	η (%)
1^{o}C/min	0.705	7.33	0.64	3.31
2^{o}C/min	0.72	7.2	0.56	3.11
one step	0.695	5.73	0.500	2.40
as deposited	0.67	1.61	0.49	0.53

As seen in table 4.2, the DSSCs whose working electrodes were annealed at 1 ^{O}C/minute had the highest PCE of 3.31 % followed by the ones annealed at 2 ^{O}C/minute with PCE of 3.11 %. Lowering and improving annealing rate is noted to improve the performance of the solar cell. The four main DSSCs parameters, J_{sc}, V_{oc}, FF and η improved with the reduction in the annealing rate. A similar trend is observed in the FF where the DSSCs made from working electrodes annealed at 1 ^{O}C/min had the highest fill factor.

Figure 4.6 shows the I-V characteristics curves of the differently annealed WEs, under a simulated sunlight of 100 mW/cm^2. I-V curves are noted to follow similar trend of change in current density to voltage.

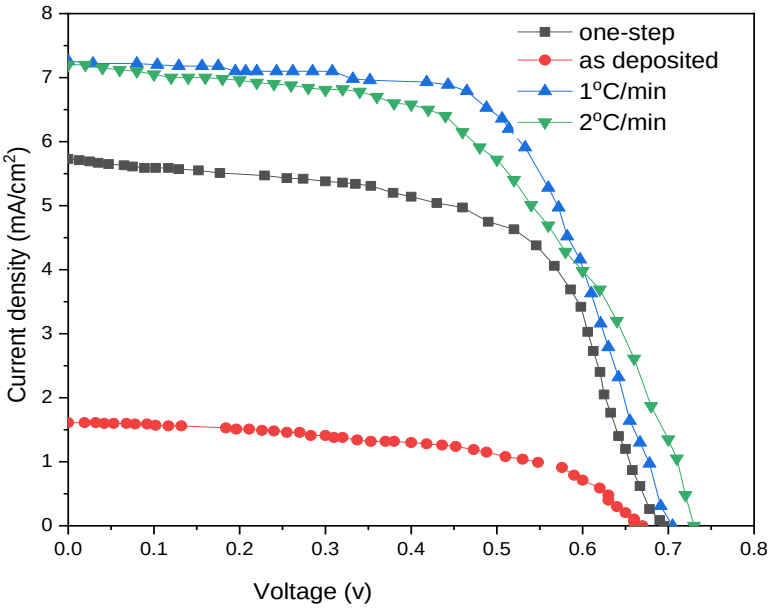

Figure 4.6: I-V Characteristics for TiO2 Thin Films Deposited onto FTO with Different Annealing Rates

The PV parameters increase gradually as the annealing rate is reduced from one step annealing at 450 ^{O}C for 30 minutes to 1 ^{O}C/minute. Solar cells with WEs annealed at 1 ^{O}C/minute have the highest J_{sc}, V_{oc}, FF of 7.33 mA/cm^2, 0.705 V and 0.64 % respectively. In comparison to as deposited WEs, 1 ^{O}C/minute samples showed an improvement of 355.28 %, 5.22 % and 30.61 % in J_{sc}, V_{oc}, and FF respectively. In the I-V curve, the tangent slope of vertical part near the V_{oc} is proportional to the reciprocal of the series resistance (1/R$_s$) (Gong *et al.*, 2012). The I-V curves demonstrate a direct relationship between the R$_s$ and J_{sc} in that the lower the series resistance, the higher the J_{sc}. In this regard, DSSCs made from WEs left to dry at ambient temperature had the highest R_s and WEs annealed at 1 ^{O}C/minute had the lowest R_s. The J_{sc} is mainly influenced by dye adhesion on the TiO_2 nanoparticles and charge recombination at the WE (Yang *et al.*, 2012). Thus, higher J_{sc} in the WEs annealed at 1 ^{O}C/minute had the

best dye adhesion and least charge recombination sites while the WEs left to dry at ambient temperature had poor dye adhesion and most recombination sites. The high values of J_{sc} denoted minimal recombination centers in the semiconducting TiO_2.

Experimentally, as the annealing rate is altered, there are expected changes in surface roughness and optical properties of TiO_2. These changes impact on the performance of the DSSCs (Habibi *et al.,* 2007). The process of eliminating water, solvents (mainly alcohols) and organic components during drying process affect the end surface roughness, optical property and adhesion of the TiO_2 on the FTO substrate (Sedghi *et al.,* 2015). Therefore, the diversified performance of DSSCs as a result of different annealing rates can be attributed to change in structural and morphological properties of the WEs. The WEs annealed at 1 ^{O}C/minute had improved surface roughness for excellent dye adhesion. The good uniformity of WEs annealed at 1 ^{O}C/minute showed increased crystallinity of the films which resulted to reduction of charge carrier trapping hence excellent electron transfer channels. Such improved crystallinity of TiO_2 is characterized by low E_g and moderate transmittance as noted in 1 ^{O}C/min WEs. The enhanced electron transfer kinetics is as a result of enhanced film quality as reported by (Tricoli *et al.,* 2012; Sedghi *et al.,* 2015). As noted earlier, there were no observable cracks and patches (grain boundaries) in the WEs annealed at 1 ^{O}C/minute. The film was uniform and produced the best DSSCs which had a FF of 64 % unlike one step annealed WEs. This is 8 % increase from the 56 % FF in the 2 ^{O}C/minute annealed WEs and 24 % increase from one step annealed. WEs annealed at 2 ^{O}C/minute had no cracks and their surface was homogeneous and have improved surface roughness. When the annealing rate increased to 450 ^{O}C for 30 minutes (one step annealing), the TiO_2 film surface became discontinuous and cracks were common. The large grain boundaries and discontinuity of one step annealed samples acted as charge recombination centers and resistance area hence the poor PV parameters. The cracking in one step annealed WEs is attributed to thermal shock as a result of the rapid evaporation of water, solvents and alcohols from the bottom part of the TiO_2 as the temperature rose above the drying temperature (~175 ^{O}C) before they could fully evaporate.

The organics usually fully evaporate at elevated temperatures of within 300 ^{O}C to 450 ^{O}C (Schattauer *et al.,* 2012). The transfer of the photo-excited electrons to the external circuit thus experienced high resistance due to the cracks which amplified the recombination process (Tricoli *et al.,* 2012). The rapid temperature increase in one step annealed samples resulted to poor film microstructure with weak adhesion on the FTO. Similar observation has been reported in that the weak TiO_2 film cohesion on the FTO leads to poor PV performance (Tricoli *et al.,* 2012). Further, the TiO_2/FTO interface resistance was high in the one step annealed WE. Poor TiO_2 film adhesion would lead to the redox couple coming into direct contact with the FTO and hence not only reducing the TiO_2 –FTO contact area but also amplifying the rate of recombination in the WEs (Kopidakis, 2004). This contributes to reduced PV parameters in one step annealed WEs. The PV improvement from in DSSCs made from WEs annealed at 1 ^{O}C/minute can thus be attributed to the enhanced film morphology of highly ordered TiO_2 surface roughness, enhanced cohesion of the film on FTO and enhanced dye adhesion on the TiO_2 (Dhunge & Park, 2013). The Highly ordered crack free TiO_2 structure is favorable for optical absorption and electron kinetics in the WEs and enhances energy conversion (Yu *et al.,* 2009; Sun *et al.,* 2012). It is expected that WEs annealed at 1 ^{O}C/minute, had open nano-channels and a nano-matrix characterized by high surface area for dye adhesion and a rapid photo-electro redox reaction for regenerating the dye hence inhibiting recombination chances.

The observed drop of E_g of annealed TiO_2 affects the performance of a DSSC. Low E_g of 2.8 eV that was achieved by annealing the TiO_2 at 1 ^{O}C/min has improved performance. The low E_g causes faster electron photo excitation that improved the performance of the solar cell (Dea *et al.,* 2024). A reduction in E_g of annealed TiO_2 at 1 ^{O}C/min can also increase the adsorbance of dye that would ensure more photons is harvested that eventually improved the overall conversion efficiency of the DSSC (Yue *et al.,* 2002). Smaller E_g can lead to an easier charge transfer process, which increases charge carrier photo generation within the solar cell and improving on the overall performance (Dea *et al.,* 2024).

During the sintering process, the porosity of the TiO_2 film is enhanced. Annealing at low temperature leads to electron trapping by the surface states leading to recombination and long electron diffusion time. This leads to a high charge transfer resistance in the electrode (Hamadanian & Jabbari, 2014). Annealing at 450 ^{O}C enhances the crystallinity of the film hence significantly reducing the charge transfer resistance due to decrease in the density of states. However, at higher temperatures, there is usually decreases the internal surface area and collapsing the porous structure. New surface states emerge on the surface of the TiO_2 which increase the charge transfer resistance again (Hamadanian & Jabbari, 2014).

4.3 Graphene Based CEs

4.3.1 Optical Transmittance of Gr Based CEs

The optical transmittance of single layer, double layer and multi-layer graphene on FTO was measured at wavelength of 300-800 nm, with offsetting to that of blank FTO. The transmittance of graphene layers is observed to increase with increase in the wavelength from 300 nm to 680 nm; however, with longer wavelengths of more than 700 nm, transmittance reduces for all CEs. All samples show similar trend and optical transmittance is found to reduce with increase in graphene layers on FTO as given in figure 4.7.

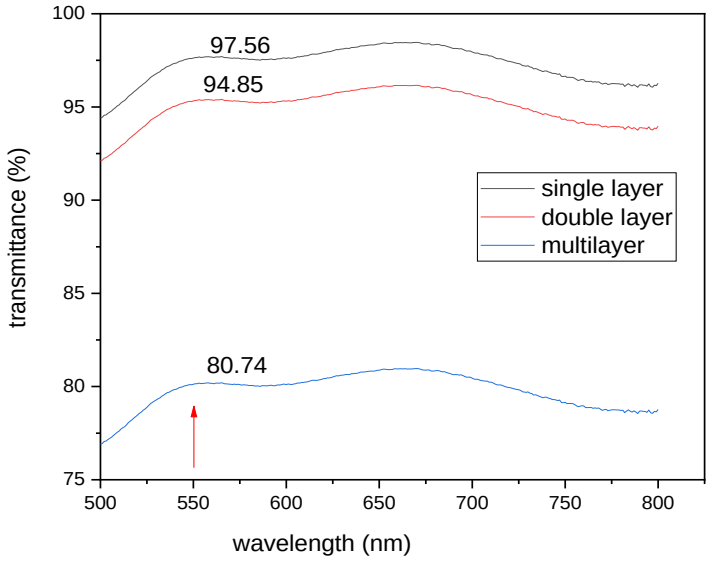

Figure 4.7: Transmittance of Single Layer, Double Layer and Multi-Layer Gr

Few layered graphene has high optical transparency, above 80 %, within the visible and near infrared region (400 – 800 nm). At normal incidence of 550 nm the transmittance of single layer, double layer and multi-layer was found to be 97.56, 94.85 and 80.74 % respectively. From these results, single layer graphene exhibits high transmittance with opacity of ~ 2.4 %, which is slightly higher than theoretical value of 2.3 %, which can be attributed to graphene's unique electronic structure (Li *et al.,* 2008). Transmittance of graphene layers was found to reduce with increase in graphene layers with each layer increase in graphene layers corresponds to a decrease of 2.4 % in the optical transmittance of these films (Li *et al.,* 2008). Such high transmittance of few layered graphene together with its electrical, thermal conductivities and mechanical properties makes it possible for them to be applied as CEs in a DSSC (Wang *et al.,* 2013). The experimental results of this work agree with reported works by Sheehy *et al.,* 2009 and Zhu *et al.,* 2014. The number of graphene layers on MLG was determined using transmittance at normal incidence 550 nm of 80.74 % with the application of equation 2.10 to be 9 (Zhu *et al.,* 2014).

Transmittance spectra of bare FTO, single layer graphene, double layer graphene and multi-layer graphene layers on FTO CE was obtained from 280 nm to 800 nm. The transmittance of both bare FTO and Gr on FTO CEs increases with change in wavelength from 300 nm to 800 nm. At shorter wavelengths, below 280 nm, the transmittance is observed to be low for all samples. With the increase in graphene layers from single layer, double layer then few layers on FTO, the optical transmittance is noted to reduce as shown in figure 4.8.

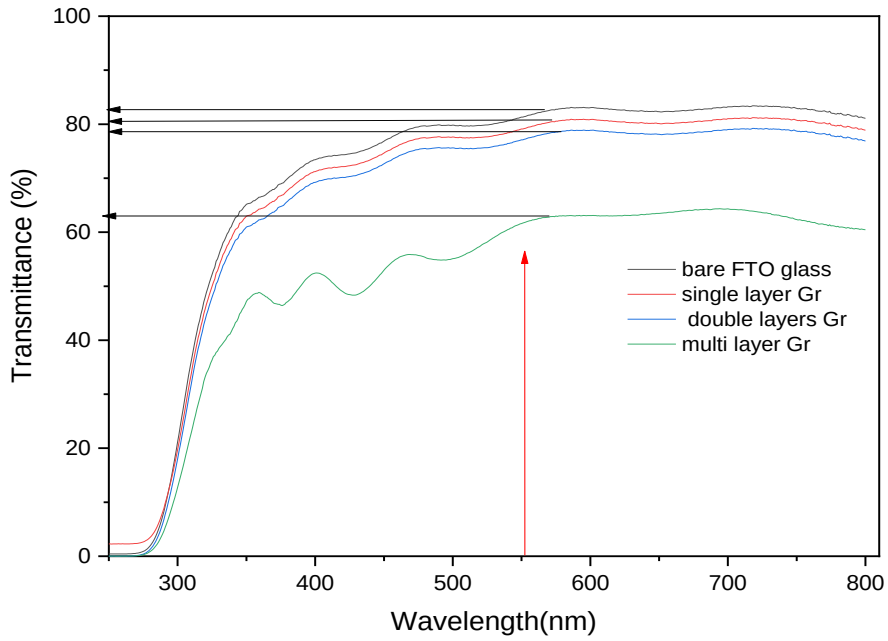

Figure 4.8: Transmittance Spectra of Bare FTO Glass, Single, Double and Multi-Layer Graphene on FTO Glass

At normal incidence of ~ 550 nm all sample show maximum transmittance with bare FTO, single layer, double layer and multi-layer on FTO having 83, 80, 78, and 60 % respectively. The transmission of graphene displays the expected optical density of ~2.3 % with reference to the bare FTO. Further, the transmittance trend of graphene on FTO to that of the bare FTO is similar depicting that graphene-FTO interface does not cause optical interference. The transmittance of graphene was found to drop with the increase

in the number of layers, with multilayer graphene on FTO giving the lowest transmittance that is below 70 %. Single layer and double layer on FTO are highly transparent in the visible-UV range. High transmittance of few layers of graphene on FTO is significant for DSSC in allowing the movement of incident sunlight down to the active region of DSSC photoanode (Wang *et al.*, 2013; Gong *et al.*, 2012; Hong *et al.*, 2008). Graphene can absorb light of wavelength range from 200 to 800 nm and therefore the addition of graphene layers caused an increase of light absorbance thus reducing the transmittance as observed.

Platinum on graphene-based CEs transmittance spectra were obtained from 280-800 nm and all samples exhibit similar trend. At shorter wavelength the transmittance is observed to be low. However, with the increase in wavelength the transmittance of all samples increases as shown in figure 4.9.

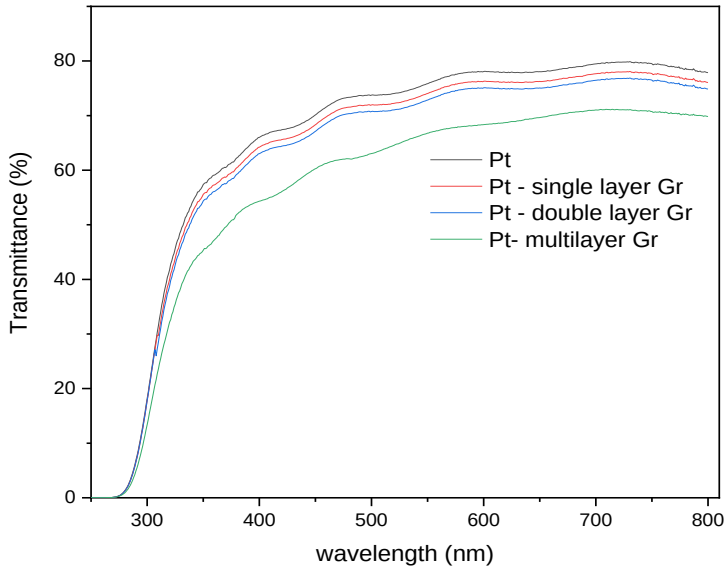

Figure 4.9: Transmittance Spectra of Bare FTO, Platinum Deposited on FTO and Pt on Single, Double and Multilayer Graphene Using Doctor Blade Method

From 350-400 nm, all the four samples indicate transient instability, caused by excitation and cross relation of the FTO atoms. Beyond 450 nm, the three samples

experienced dynamic stability (Katumo *et al.,* 2015). The average transmittance was calculated to be 78.25 %, 76.61 %, 73.81 % and 65.43 % for Pt on FTO, Pt on single layer Gr, Pt on double layer graphene and Pt on multi-layer Gr on FTO respectively in the dynamically stable region of 450-800 nm. It can also be observed that there is no optical interference that occurs when platinum is interfaced with graphene within the visible and near infrared region (NIR) (400-800 nm). The transmission curves however coincide at the extremes, both within the ~300 nm range and the ~800 nm range indicating reduced transmission of ultraviolet and NIR radiation (beyond ~800 nm). This is mainly caused by the FTO glass substrate which undergoes transient instability within these wavelength ranges hence absorbing almost all the incident radiations. The highest optical transmittance of graphene and Pt-Gr CEs is maximum at 750 nm with the Pt CE indicating a transmission of 78.5 % whereas Pt on single layer Gr CE and Pt-double layer Gr having a transmission of 77.3 % and 75.4 % respectively. The high and constant transmittance of 70 % in the most of the visible range of the spectrum indicates that platinum on graphene layers CE's can be used for rear illumination and in window application.

4.3.2 Electrical Properties of Graphene Layers

Sheet resistance of graphene on conductive substrate FTO was evaluated using four-point probe by taking four equally spaced, co-linear probes (1 inch × 1 inch) to make electrical contacts on graphene deposited on FTO. Sheet resistance was observed to be high on single layer graphene on FTO and low on multi-layer graphene on FTO as given in figure 4.10.

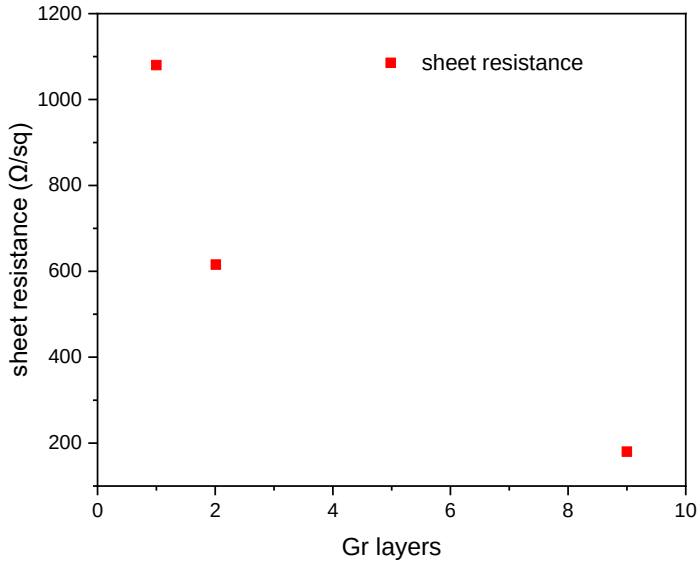

Figure 4.10: Variation of Rs (Ω/sq) with Graphene Layers on FTO

Sheet resistance of single layer, double layer and multi-layer Gr on FTO was found to be 1100, 620 and 180 Ω/sq respectively. Single layer Gr offers high R_s with multi layer Gr having the lowest. From the results it can be noted that R_s reduces with increase in number of graphene layers (Wang *et al.,* 2011). Reduction of R_s leads to increase in conductance of the films which is beneficial in photovoltaic application (Singh & Hari, 2015).

4.4 I-V Characteristic Curve for DSSC Fabricated using Platinum on Gr CEs

Photocurrent voltage curves for DSSCs fabricated from Pt, Pt on graphene layers-based CEs with WEs annealed at 1 ^{O}C/min are shown in figure 4.11. I-V curves obtained are observed to follow typical trend for DSSCs. Incorporating graphene on platinum-based CEs is observed to affect J_{sc}, V_{oc}, FF and η of DSSCs.

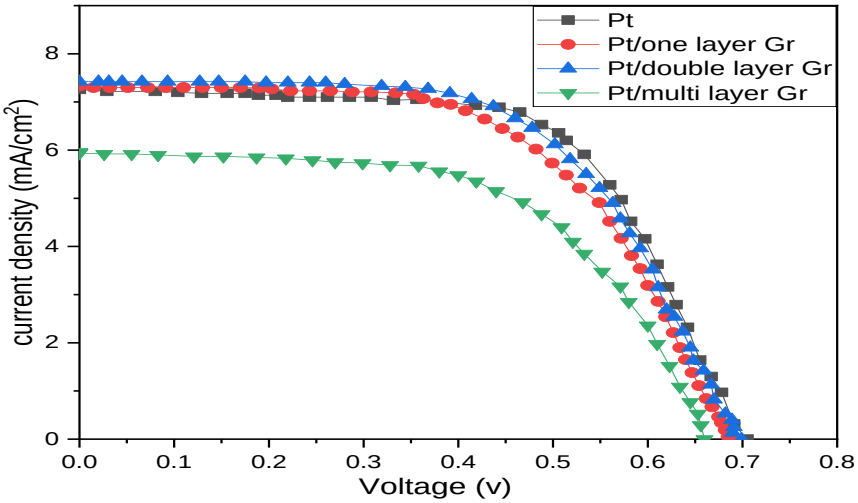

Figure 4.11: The Photocurrent Density-Voltage Curves of Pt on Graphene Layers CE's and Reference Pt DSSCs.

Photovoltaic parameters that are summarized in table 4.3. Few graphene layers on platinum-based CEs are noted to improve on the FF, *Jsc*, *Voc*, and η of DSSCs.

Table 4.3: Photovoltaic parameters Pt on Graphene Layers and Pt Based CEs DSSCs

Sample	V_{OC} **(v)**	J_{SC} **(mA/cm^2)**	***F.F* (%)**	P_{max} **(mW/cm^2)**	η **(%)**
Pt	0.71	7.26	0.63	5.15	3.25
Pt/single-layer Gr	0.69	7.50	0.635	5.17	3.30
Pt/double-layer Gr	0.70	7.62	0.64	5.33	3.41
Pt on multi-layer Gr	0.66	5.96	0.55	3.93	2.16

Comparing the maximum output power, Pt on double layer Gr CEs gives the highest maximum power of 5.33 mW/cm^2. Pt on single layer Gr CEs improves J_{sc} from 7.26 to 7.50 mA/cm^2, FF slightly changing from 0.63 to 0.635 and also conversion efficiency improving from 3.25 to 3.30 %. Incorporation of multi-layer Gr on Pt CEs, give relatively low values of V_{oc}, J_{sc}, FF and overall conversion efficiency. The observable difference in the fabricated DSSCs is on *Jsc* and PCE but there is no significant

variation in both the V_{oc} and FF. Pt on few layers Gr, single and double layers, improve on the J_{sc} and hence on the overall conversion efficiency. This improvement can be attributed to high transmittance of both single layer and double layers of graphene films as observed (Das *et al.,* 2014). The conversion efficiency of DSSC is observed to increase with increase of graphene layers from single layer to double layer then drop with MLG on pt counter electrode. Incorporating single layer graphene on platinum improves η from 3.25 to 3.30 % and double layer improve from 3.25 to 3.41 %. Pt on double layer Gr increases the conversion efficiency by ~ 5 %. Pt on multi-layer graphene gives lower conversion efficiency as compared to Pt on double layer graphene which offer better performance.

Surface resistance of the graphene sheets is very important in a DSSC, as sheet resistance determine the resistance of the electrons in the cell, influencing directly on the efficiency of the DSSC (Das *et al.,* 2014, Li *et al.,* 2013)). As noted from the results, with the reduction of sheet resistance, from 1100 to 620 Ω/sq, the conversion efficiency of solar cells of graphene on platinum-based CEs, improves from 3.30 to 3.41 %. MLG on FTO was noted to have improved R_s of 180 Ω/sq but conversion efficiency was found to be low, 2.16 %, which can be attributed to low transmittance (insolation) as compared to single- and double-layers Gr that have high transmittance.

From the Rs obtained, Pt on double layer graphene with low sheet resistance has the highest J_{sc} and improved performance of the cell. Based on sheet resistance, sheet conductance and high transparency of CEs, the performance of a solar cell can be determined (Das *et al.,* 2019). For maximum DSSC efficiency, the sheet resistance should be small and optical transmittance should be large as noted in Pt on double layer graphene CEs. With an increase in the number of graphene layers, both the optical transmittance and sheet resistance decrease (sheet conductance increases) as earlier noted. Thus, sheet resistance and optical transmittance are two competing parameters for high efficiency of graphene-based CEs. The enhanced conductivity of graphene film is good for the increase of J_{sc} and reducing the internal resistance of the solar cell. The observed drop in sheet resistance from single layer to double layer Gr on FTO is

beneficial to the performance of DSSC, because it improves the J_{SC}, FF and η (Singh & Hari, 2015; Tasis, 2017). In this work, Pt on double layer Gr was found to have good conductivity and appropriate transparency that is required for better performance of a DSSC. This is consistent with reports by Wang *et al*., 2011 who demonstrated a proportional decrease in optical transparency (transmittance) with an increase in graphene layer number from 1 to 8. Reports have also noted the decrease in series and sheet resistance of graphene structure with graphene's rising number of layers (Wang *et al.*, 2011; Li *et al.*, 2008; Zhu *et al.*, 2014). However, although the nature of variation remains the same, the exact amount of reduction in transmittance, variation in R_S, series resistance, shunt resistance, V_{oc}, J_{sc}, FF and η with graphene thickness is purely subjective to the consecutive layers of graphene layer. Double layer and tri-layer graphene, in most cases, offer high efficiency attributed to their adequate transparency as well as sheet conductance (Li *et al.*, 2014; Das *et al.*, 2014; Phaedon, 2010).

When Pt is contacted to graphene, Pt develops a negative surface charge which is favorable for its catalytic activity in the reduction of the electronegative triiodide. This is due to the work function (WF) difference between the two materials, with graphene having ~ 4.6 *eV* and platinum having ~5.7 *eV* (Gossenberger *et al.*, 2014; Seo *et al.*, 2014). The 1.1 *eV* WF difference causes surface charges which enhance triiodide reduction on the platinum surface. As a result, when a Pt/Gr interface is formed, electrons migrate from the low WF metal (graphene) to the high WF metal (Pt) (Gossenberger *et al.*, 2014). This leads to electron tunneling due to the surface dipole which supplements the normal electrochemical process in the electrode-electrolyte interface (Gossenberger *et al.*, 2014).

The charge transfer creates a negative surface potential on the Pt surface which favors backward electron transfer kinetics (Yen *et al.*, 2011; Yue *et al.*, 2013). This leads to the electronegative redox couple triiodide species picking electrons easier as compared to the case of absence of a negative surface potential. The picked electrons on the Pt surface are easily replaced by the superconducting graphene (Yue *et al.*, 2013). This phenomenon leads to enhanced catalytic activity of platinum on graphene layers and

reduced recombination due to high concentrations of I_3^- (Boschloo *et al.,* 2009). The electronegative Pt surface of Pt/Gr CE has been reported to have low contact resistance compared to the bare Pt based CE (Cheng *et al.,* 2013; Gong *et al.,* 2011; Yen *et al.,* 2011; Sur *et al.,* 2012). Further, graphenes' high electrical conductivity and high specific area property as opposed to FTO surface has been reported to enhance Pt catalytic activity (Cheng *et al.,* 2013; Sur *et al.,* 2012; Yue *et al.,* 2013). It has been reported that, the platinum film on graphene is sufficiently dispersed and stabilized for maximum accessibility of the electrolyte (Tan *et al.,* 2013; Neto *et al.,* 2009; Garg *et al.,* 2014). Further, the diffusion of the redox species in the pores of platinum is maximized by the increased surface area of Pt resting on graphene (Seger *et al.,* 2009; Gong *et al.,* 2011).

The high value of Pt WF is core in ensuring the surface has sufficient electrons for fast reduction of the redox species when the Pt on Gr interface is formed. Thus, the high *Jsc* in Pt on Gr is ascribed to the introduced surface charge potential that leads to enhanced catalytic activity. The Pt/Gr also provides larger diffusion coefficient leading to a facile electron transfer hence the high J_{sc} (Yue *et al.,* 2013).

Thus, through introducing the Pt/Gr interface, the electrochemical processes that occur in the counter electrode is supplemented by electron tunneling thus availing more electrons for the reduction of the triiodide. These propositions are consistent with what has been previously reported by Gong *et al.,* 2011; Yen *et al.,* 2011; Yue *et al.,* 2013.

CHAPTER FIVE

CONCLUSIONS AND RECOMMENDATIONS

5.1 Conclusions

Annealing rates of TiO_2 films as WE for DSSC was found to influence the surface roughness and optical properties of TiO_2 thin films. TiO_2 annealed at optimized rate of 1 ^{O}C/min have improved surface roughness with no cracks and agglomeration as compared to one step annealed at 450 ^{O}C for 30 minutes that were characterized by cracks and defects such as globules and agglomeration. Low annealing rates (1 ^{O}C/min) lowers transmittance, improves both absorbance and band gap of TiO_2 thin films which increased dye adhesion, photon absorption and lower charge recombination at the WEs and eventually improve the conversion efficiency of the DSSC.

Pt on Gr layers was noted to have high transmittance in the visible region of light spectrum. Addition of graphene layers reduces the sheet resistance and improves the sheet conductance of Pt based CEs. Pt on double layer Gr was found to have improved sheet resistance, 620 Ω/sq, and appropriate transparency for better performance of a DSSC. Incorporation of single and double layer Gr on Pt based CEs improved J_{SC}, FF, and η. Pt on double layer Gr improves J_{sc} from 7.26 to 7.62 mA/cm^2, FF from 0.63 to 0.64 and η from 3.25 to 3.41% from Pt reference DSSC. Pt on double layer Gr showed the best improvement in η of 5 % as compared to Pt on single layer Gr and Pt on multi-layer Gr.

5.2 Recommendations

1. Annealing rates of the TiO_2 film were demonstrated to affect the PV performance of DSSCs. Based on the results; we recommend further investigation on the effect of low annealing rates, 1 ^{O}C/min, on homogeneity, porosity, and structure of TiO_2 thin films as WEs in the performance of DSSC. Advanced morphological and surface characteristic measuring instruments such

as Scanning Electron Microscope (SEM) and Tunneling Electron Microscope (TEM) should be used in the analysis.

2. The results of this study on the influence of graphene layers on the photovoltaic performance of platinum-based CEs are promising in the field of solar cells. We recommend that Pt on Gr films on FTO as CEs be structurally, electrically and morphologically characterized to unravel the cause of PCE enhancement. Further studies therefore should be taken on correlation of coverage and structure of graphene layers on FTO substrates to its conductivity as CEs of DSSCs. Further studies should also be done on structural and electrochemical characteristics of platinum supported on graphene sheets as CEs that affect the catalytic activity in DSSCs.

REFERENCES

Arbab, A.A., Sun, K.C., Sahito, I.A., Qadir, M.B., Jeong, S.H.J.P.C.C.P., (2015). Multiwalled Carbon nanotube coated polyester fabric as textile based flexible counter electrode for Dye sensitized solar cell. *Journal of physical chemistry*. *17*(19), 12957–12969.

Avouris, P. (2010). Graphene: Electronic and Photonic Properties and Devices. *Nano Letters, 10* (11), 4285.

Benjamin, M. J., Simon, W. M., & James, M. N. (2018). Effect of Annealing Rates on Surface Roughness of TiO_2 Thin films. *Journal of Materials Physics and Chemistry*, *6*(2), 43-46.

Böer, K. W. (2002). Survey of Semiconductor Physics II. *Springer nature,*13-15.

Boschloo, G., & Hagfelt, A. (2009). Characteristics of the iodide/triiodide redox mediator in dye Sensitized Solar Cells. *Acc. Chem. Res. 42*, 1819-1826.

Brown, P., & Kamat, P. V. (2008). Quantum dot solar cells. Electrophoretic deposition of CdSe-C60 composite films and capture of photogenerated electrons with nC60 cluster shell . *J. Am Chem. Soc., 130*(28), 8890–8891.

Chapin, D. M., Fuller, C. S., & Pearson, G. L. (1954). A new silicon p-n junction photocell for converting solar radiation into electrical power. *Journal of applied physics, 25*(5), 676–677.

Cheng, C., Lin, C., Shan, C., Tsai, S., Lin, K., Chang, C., & Chien, S. (2013). Platinum-graphene counter electrodes for dye sensitized solar cells. *Journal of applied physics, 114*, 014503.

Cheng, C.-E., Lin, Z.-K., Lin, Y.-C., Lei, B.-C., Chang, C.-S., & Chien, F. S. (2016). Pt crystalline ultrathin films as counter electrodes for bifacial dye-sensitized solar cells. *Japanese Journal of Applied Physics, 56*(1).

Chergui, Y., Nehaoua, N., & Mekki, D. E. (2010). Comparative Study of Dye-Sensitized Solar Cell Based on ZnO and TiO_2 Nanostructures. *Solar cells, 2*, 50-57.

Choi, W., & Lee, J. (2011). *Graphene: Synthesis and Applications*. CRC Press.pp.3-7

Corporation, S. (2015). Sample cell selection guide for spectroscopy applications. Retrieved from http://www.ssi.shimadzu.com/products/literature/Spectroscopy/ Shimadzu_ CuvetteGuide_2014.pd.

Das, S., Pandey, D., Thomas, J., & Roy, T. (2019). The role of graphene and other 2D materials in solar photovoltaics. *Adv. Mater, 31*, 1802722.

Das, S., Sudhagar, P., Kang, Y., & Choi, W. (2014). Graphene synthesis and application for solar cells, *Adv. Mater*., *29*(3), 299-319.

Dea, A.K., Nabella, S., Nanda, N.K., Markus, D., Arif, N.A., Zurina, O.,, Herlin, P (2024). Ag- doped TiO_2 as photoanode for high performance dye sensitized solar cells. *Materials Science for Energy Technolo*gies, *7*, 274-281.

Dhunge, S., & Park, C. (2013). Impact of size distribution of nanoparticles in TiO_2 paste for its application in dye sensitized solar cells. *Himalayan Physics*. *4*(4), 27-31.

Dodoo-Arhin, D., Fabiane, M., Bello, A., & Manyala, N. (2013). Graphene: Synthesis, transfer, and characterization for dye sensitized solar cells applications. *Ind. Eng. Chem. Res.*, *52*, 14160-14168.

Dou, Y. Y., li, G. R., J, s., & Gao X, P. (2012). Nickel phosphide-embedded graphene as counter electrode for dye-sensitized solar cells. *Physical Chemistry Chemical Physics, 14*, 1339-1342.

Enoki, T., & Ando, T. (2013). Physics and Chemistry of graphene: Graphene to Nanographene. *Jenny Stanford Publishing*, 1212-127. https://doi.org/10.1201/b14396

Garg, R., Dutta, N., & Choudhury, R. (2014). Work Function Engineering of Graphene. *Nanomaterials*, *4*, 267-300.

Geim, K. (2009). Status and Prospects. *Science*, *324*(5934), 1530–1534.

George, C., & Nathan, L. (2007). Solar energy conversion. In Physics of Sustainable Energy: Using Energy Efficiently and Producing It Renewably: Berkeley, California, Melville, NY, *American Institute of Physics .4*(45), 36–42.

Green, M.A., Dunlop, E.D.; Hohl-Ebinger, J., Yoshita, M., Kopidakis, N., Bothe, K., Hinken, D.; Rauer, M. & Hao, X. (2022). Solar cell efficiency tables (Version 60). *Prog. Photovolt. Res. Appl., 30,* 687–701.

Gong, F., Wang, H., & Wang, Z. (2011). Self-assembled monolayer of graphene /Pt as a counter electrode for efficient dye-sensitized solar cell. *Phys. Chem. Chem. Phys.*, *13*, 17676-17682.

Gong, J., Liang, J., & Sumathy, K. (2012). Review on dye-sensitized solar cells (DSSCs). *Fundamental concepts and novel materials, 16,* 5840-5860.

Gossenberge, r. F., Roman, T., Forster-Tornigol, K., Grob, A., & Behm, R. (2014). Change of the work function of Platinum electrodes induced by halide adsorption. *Beilstein J Nanotechnol*., *5*, 152-161.

Grätzel, M. (2003). Dye-sensitized solar cells. *Journal of Photochemistry and Photobiology Cs*., *4*(2), 145–153.

Gratzel, M. (2003). Photochemistry Reviews. *Photochemistry and Photobiology C. 4*, 145-153.

Green, M. (2017). "Solar cell efficiency tables (version 50*)." Progress in Photovoltaics: Research and Applications, 25*(7), 668-676).

Guo, H., Wan, X., Qian, Q., Wang, F., & Xia, X. (2009). A green approach to the synthesis of graphene nanosheets. *ACS Nano, 3*(9), 2653-2659.

Habibi, M., Talebian, N., & Choi, J. (2007). The Effect of Annealing on Photocatalytic Properties of Nanostructured Titanium Dioxide Thin Films. *Dyes and Pigments. 73*, 103-110.

Hamadanian, M., & Jabbari, V. (2014). Improved conversion efficiency in dye-sensitized solar cells based on Electrospun TiCl4-treated TiO2 nanorod electrodes. *International Journal of Green Energy*, *11*(4), 364-375.

Hassan, M., Haseeb, A., Saidur, R., & Masjuki, H. (2008). Effects of Annealing Treatment on Optical Properties of Anatase TiO_2 Thin Films. *World journal of nuclear science and technology*. *40*, 221-225.

Hemamali, G. N., & Kumara, G. R. (2013). Solid State Solar Cells Based On TiO2 Sensitized With Natural Pigment Extracted From the Anthurium. *International Journal of Scientific and Research Publication, 3*(12), 2–6.

Hong, W., Xu, Y., Lu, G., Li, C., & Shi, G. (2008). Transparent graphene/PEDOT-PSS composite films as counter electrodes of dye-sensitized solar cells . *Electrochemistry communications, 10*(10), 1555–1558

Mikhail K.I (2012). Graphene as a Prototype Crystalline Membrane. *ACS , 46*(1).

IUPAC. (1997). Amount concentration, c. In *the Gold Book. Compendium of Chemical Terminology,* (2nd ed.). pp.1-3

Jasim, K. E. (2007). Dye sensitised solar cells-working principles, challenges and opportunities. *Material science*, 175-204.

Jayawardena, K., Rozanski, L., Mills, C., Beliatis, M., Nismy, N., & Silva, S. (2013). Inorganic-in-organics: recent developments and outlook for 4G polymer solar cells . *nanoscale, 5*, 8411-8427.

Kang, M., Park, N., Chang, S., Choi, S., & Kim, K. (2015). Rose Bengal sensitized bilayered photoanode of nano-crystalline TiO_2–CeO_2 for dye-sensitized solar cell application. *Applied Nanoscience, 6*, 875-881.

Katumo, N., Mugo, S. W., Ngaruiya, J. M., Ngumbi, P. K., & John, M. (2015). Graphene Supported Platinum Counter Electrode for Dye Sensitized Solar Cells. *Ijirset*, *4*(12), 12251–12258.

Kim, S., Park, J., Kim, C., Okuyama, K., Lee, S., Jang, H., & Kim, T. (2015). Effects of graphene in dye-sensitized solar cells based on nitrogen doped TiO_2 composite. *Material science, 119*(29), 16552-16559.

Kim S. S., Nah Y. C., Noh Y. Y., Jo J. and D. Y. Kim D.Y, (2006). Ectrodeposited Pt for cost-efficient and flexible dye-sensitized solar cell Electrochim. Acta, *51*, 3814–3819

Koo, H., Park, J., Yoo, B., Yoo, K., Kim, K., & Park, N. (2008). Size-dependent scattering efficiency in dye-sensitized solar cell. *Inorg Chim Acta, 361*, 677-683.

Kopidakis, N., Van de Lagemaat, J., & and Frank, A. J. (2004). Electrons in nanostructured TiO_2 solar cells: transport, recombination and photovoltaic properties. *Coordination chemistry review, 248*, 1165).

Lee, J., Yoon, D., & Cheong, H. (2012). Estimation of Young's modulus of graphene by Raman Spectroscopy. *Nanoletters, 12*(9), 4444-4448.

Lemme, M. C. (2010). Current status of graphene transistors. *Solid state phenomenon, 156-158*, 499-509.

Li, S., & Zhang, C. (2013). First-principles study of graphene adsorbed on WS_2 monolayer. *Journal of applied physics*, *114*(183709), 1-6.

Li, Z., Henriksen, E., Jiang, Z., Hao, Z., Martin, M., Kim, P and Basov, N. (2008). Dirac charge dynamics in graphene by infrared spectroscopy.*nature physics*, *4*, 532-535.

Lim, J., Ryu, S. Y., Kim, J., & Jun, Y. (2013). A study of TiO_2/carbon black composition as counter electrode materials for dye-sensitized solar cells. *Nanoscale Res Lett*., *8*(1), 277.

Listanti, A., Taufiq, A., Hidayat, A., & Sunaryono, S. (2018). Investigating Energi Band Gap of Nano TiO2 - Sol-Gel JPSE. *Journal of Physical Science and Engineering, 3*(1), 8-15.

Matte, H., Subrahmanyam, K., & Rao, C. (2011). Synthetic aspects and selected properties of graphene. *Nano materilas*. *1*(1), 3-13.

Mohammed, A., Ahmad, A., & Azeez, W. (2015). Fabrication of Dye Sensitized Solar Cell Based on Titanium Dioxide (TiO_2). *Advances in Materials Physics and Chemistry* (5), 361-367.

Muaz, A. K., Hashim, U., Arshad, M. M., Ruslinda, A. R., Ayub, R. M., Gopinath, S. C., & Foo, K. L. (2016). Effect of annealing temperature on structural, morphological and electrical properties of nanoparticles TiO_2 thin films by sol-gel method. *American journal of material science, 1*(1733), 020087.

Murakami, T. N & Graetzel, M. (2008). Counter Electrodes for DSC: Application of Functional Materials as Catalysts Inorg. Chim. *Acta*, *361*, 572–580.

Naceur, J. B., Gaidi, M., Bousbih, F., Mechiakh, R., & Chtourou, R. (2012). Annealing effects on microstructural and optical properties of nanostructured-TiO2 thin films prepared by sol–gel technique. *Current applied physics 12*(2), 422-428.).

Nair, R., Black, P; Grigorenko, A., Novoselov, k & Booth, T (2008). Fine Structure Constant Defines Visual Transparency of Graphene. *Science, 320*(5881), 1308.

Nam, J. G., Park, Y. J., Kim, B., & Lee, J. S. (2010). Enhancement of the efficiency of dye-sensitized solar cell by utilizing carbon nanotube counter electrode. *Scripta meterialia*, *62*(3), 148–150.

Nazeeruddin, M. K., Péchy, P., & Grätzel, M. (1997). Efficient panchromatic sensitization of nanocrystalline TiO_2 films by a black dye based on a trithiocyanato-ruthenium complex. *Chemical communications*, *1*(18), 1705–1706

Neto, A. H., Guinea, F., Peres, N., Novoselov, K., & Geim, A. (2009). The electronic properties of graphene. *Rev. mod. Physics*, *81*, 109-162.

Neuthe, K. (2014). Synthesis and characterization of transition metal-based dyes for the application in Dye sensitized solar cells. *Coordination chemistry reviews*, *7*, 538–541.

Novoselov, S., Geim, A., Morozov, S., Jiang, D., Zhang, Y., Dubonos, S., Firsov, A. (2004). Electric field effect in atomically thin carbon films. *Science 306*(5696), 666-669.

Olsen E., Hagen G. and Lindquist S. E. (2000) Dissolution of platinum in methoxy propionitrile Containing LiI/I Sol. *Energy Mater*. Sol. Cells, *63*, 267–273

O'Regan, B., & Grätzel, M. (1991). A low-cost, high-efficiency solar cell based on dye-sensitized colloidal TiO_2 films. *Nature. 353*, 737–740).

OH, C. (2005). Measuring the resistivity and determining the conductivity type of semiconductor materials using a four-point collinear probe and the model 6221 DC and AC current source application note 2615. Keithley Instrument.

Pawar, S., Chougule, M., Godse, P., Jundale, D., Pawar, S., Raut, B., & Patil, V. J. (2011). Effect of Annealing on Structure, Morphology, Electrical and Optical Properties of Nanocrystalline TiO_2 Thin Films. *Journal of nano and electronic physics*, (3), 185.

Perdana, R., & Dahlan, D. (2013). Structure and optical properties of TitaniumDioxide thin film with mixed Fluorine and Indium doping for solar cell components. *Journal of Physic*, *6*(1), 18-24.

Phaedon, A. (2010). Graphene: Electronic and Photonic Properties and Devices. *ACS, physics and chemistry, 10*(11), 4285.

Raccichini, R., Varz, i. A., Passerini, S., & Scrosati, B. (2015). The role of graphene for electrochemical energy storage. *Science. 14*, 271-279

Ryan, M. (2009). Progress in ruthenium complexes for dye sensitised solar cells. *Plat inum Metals Review*, *53*, 216–218.

Sankar, S., & Gopchandran, K. (2009). Effect of annealing on the structural, electrical and optical properties of nanostructured TiO_2 thin films. *Crystal research and technology*, *44*, 989.

Schattauer, S., Reinhold, B., Albrecht, S., Fahrenson, C., Schubert, M., Janietz, S., & Neher, D. (2012). Influence of sintering on the structural and electronic properties of TiO_2 nanoporous layers prepared via a non-sol-gel approach. *Colloidal Polymer Science*, *290*, 1843-1854.

Sedghi, A., & Miankushki, H. N. (2015). The effect of drying and thickness of TiO_2 electrodes on the photovoltaic performance of dye-sensitized solar cells. *International journal of electrochemical, 10*, 3354-3362.

Seger, B., & Kamat, P. V. (2009). Electrocatalytic active graphene-platinum nanocomposites. Role of 2-D carbon support in PEM fuel cells. *World journal of nano science and engineering, 113*, 7990-7995.

Seo, J. K., Bong, J., Cha, J., Lim, T., Son, J., Park, S. H., Ju, S. (2014). Manipulation of graphene work function using a self-assembled monolaye. *Journal of applied physics, 116*, 084312.

Sheehy, D. E., & Schmalian, J. (2009). Optical transparency of graphene as determined by the fine-structure constant. *American physical society* (80*)*19341.1–4.

Singh, E., & Hari, S. (2015). Graphene-based bulk-heterojunction solar cells. *A review. J. Nanosci. Nanotechnol., 15*, 6237–6278.

Smits, F. (1958). Measurement of sheet resistivities with the four-point probe. *Bell Labs Tech J, 37*(3), 71118.

Stathatos, E. (2008). Dye Sensitized Solar Cells as an Alternative Approach to the Conventional Photovoltaic Technology Based on Silicon - Recent Developments in the Field and Large Scale Applications. *Solar Cells-Dye Sensitized Devices, 8*, 471–492.

Stathatos, E. (2012). Dye Sensitized Solar Cells: A New Prospective to the Solar to Electrical Energy Conversion. Issues to be Solved for Efficient Energy Harvesting. *JESTR*, *5*(4), 9–13).

Stereeman, B. (1980). Solid State Electronic Devices. *2nd Ed, Practice Hall, Inc. Engle wood Cliffs, 3*(1), 8.

Sultana, R., Abdul, H., Muhammad, S., Muhammad, K., Hussain, O., Samina, Q., Muhammad, W. (2023). Research on dye sensitized solar cells: recent advancement toward the various constituents of dye sensitized solar cells for efficiency enhancement and future prospects. *Royal society of chemistry, 13*, 19508-19529.

Sun, K.C., Memon, A.A., Arbab, A.A., Sahito, I.A., Kim, M.S., Yeo, S.Y., Choi, Y.O., Kim, Y.S., Jeong, S.H., (2018). Electrocatalytic porous nanocomposite of graphite nanoplatelets anchored with exfoliated activated carbon filler as counter electrode for dye sensitized Solar cells. *Materials, 167*, 95–101.

Sun, Z., Kin, J., Zhao, Y., Bijarbooneh, F., Malgras, V., & Xue, S. (2012). Improved phorovoltaic performance of dye-sensitized solar cells with modified self-assembling highly ordered mesoporous TiO_2 photoanodes. *Material chemisrty 22*(23), 117.

Sur, U. K. ((2012). Graphene: A rising star on the horizon of material science. *Electrochemistry*, 237689.

Tan, C., X, H., & Zhang, H. (2013). Synthesis and applications of graphene-based noble metal nanostructures. *Materilas today, 16*, 29-36.

Tasis, D. (2017). Recent progress on the synthesis of graphene-based nanostructures as counter electrodes in DSSCs based on iodine/iodide electrolytes. *Catalysts*. *7*(8), 234.

Tauc, J., Wong, M. S., P, C. H., & Yang. (1974). Thin Solid Films. *Material science, 494*(159).

Tian, G., Dong, L., Wei, C., Huang, J., He, H., & Shao, J. (2006). Investigation on microstructure and optical properties of titanium dioxide coatings annealed at various temperature. *Optical materials, 28*(8-9), 1058-1063).

Tipparach, U., Wongwanwatthana, P., Sompan, T., Saipin, T., & Krongkitsiri, P. (2008). Nanotechnology Preparation and Characterization of Nano-TiO_2 Thin Films by Sol-gel Dip-coating Method. *Nature science*, *7*(1), 129.

Tricoli, A., Wallerand, A. S., & Righettoni, M. (2012). Highly porous TiO_2 films for dye sensitized solar cells. *Material chemistry*, *22*, 14254-14261.

Wang, H., Wang, Q., Zhou, K., & H.L, Z. (2013). Graphene in light: Design, synthesis and applications of photo-active graphene and graphene-like materials. *Nano. micro small, 9*(3), 1266–1283 .

Wang, Q., Xu, Y., Iwaniczko, E., & Page, M. (2011). Light Trapping for High Efficiency Heterojunction Crystalline Si Solar Cells. *ECS transaction*, *1*, 1-9.

Wibowo, K. M., Sahdan, M. Z., Asmah, M. T., Saim, H., Adriyanto, F., & Hadi, S. (2017). Influence of Annealing Temperature on Surface Morphological and Electrical Properties of Aluminum Thin Film on Glass Substrate by Vacuum Thermal Evaporato. *Materials science and engineering*, *26*(1), 012180.

Wu, J., Lan, Z., Hao, S., Li, P., Lin, J., Huang, M., Huang, Y. (2008). Progress on the electrolytes for dye- sensitized solar cells. *Pure and applied chemistry*, *80*, 2241–2258.

Yang, R., Chen, H., & Lai, F. (2012). Performance degradation of dye-sensitized solar cells induced by electrolytes. *Adv. Mterials sci. and Eng*., 902146.

Ye, M., Wen, X., Wang, M., Iocozzia, J., Zhang, N., Lin, C., & Lin, Z. (2015). Recent advances in dye-sensitized solar cells: From photoanodes, sensitizers and electrolytes to counter electrodes. *Material today*, *18*(3), 155–162.

Yen, M., Teng, C., Hsiao, M., Kiu, P., Chuang, W., Ma, C., Tsai, C. (2011). Platinum nanoparticles/graphene composite catalyst as a novel composite counter

electrode for high performance dye-sensitized solar cells. *Material chemistry, 12*, 12880-12888.

Yu, H., Zhang, S., Zhao, H., Will, G., & Liu, P. (2009). An efficient and low cost TiO_2 compact layer for performance improvement of dye-sensitized solar cells. *Electrochimica Acta, 54*(4), 1319-1324.

Yu, J.C., Ho, W., Jiang, Z., Zhang, L (2002) Effects of F-doping on the photocatalytic activity and microstructures of nanocrystalline TiO_2 powders. *Chem Mater*, *14*(9), 3808-3816

Yue, G., Wu, J., Xiao, Y., Huang, M., lin, J., Fan, L., & lan, Z. (2013). Platinum/graphene hybrid film as a counter electrode for dye-sensitized solar cells. *Electrochimica Acta, 92*, 64-71.

Zhang, D., Li, X., Li, H., Chen, S., Sun, Z., Yin, X., & Huang, S. (2011). Graphene-based counter electrode for dye-sensitized solar cells. *Carbon, 49*(15), 5283-5388.

Zhang, J., Freitag, M., Hagfeldt, A., Boschloo, G., (2018). Solid-state dye-sensitized solar cells. In Molecular Devices for Solar Energy Conversion and Storage. *Springer*, 151–185.

Zhang, W., Li, Y., Zhu, S., & Wang, F. (2004). Photocatalytic Property of TiO_2 Films Deposited by Pulsed DC Magnetron Sputtering. *Material and technology*, *182*, 192.

Zhu, N. H., Wen, J. M., & Zhang, T. Z. (2007). Optical and Electrical Spectrum Analysis of Optoelectronic Devices. *Opto. Electronic dev.*, *1*(207).

Zhu, S. E., Yuan, S. J., & Janssen, G. (2014). Optical transmittance of multilayer graphene. *Euro physics letters*, *108*(1), 17007.

APPENDICES

Appendix I: A Photograph of a Section of the Setup of DSSCs Fabrication progress Showing, Doctor Blade of Electrode and the Final Fabricated Cell

Doctor blade technique

Fabricated solar cell

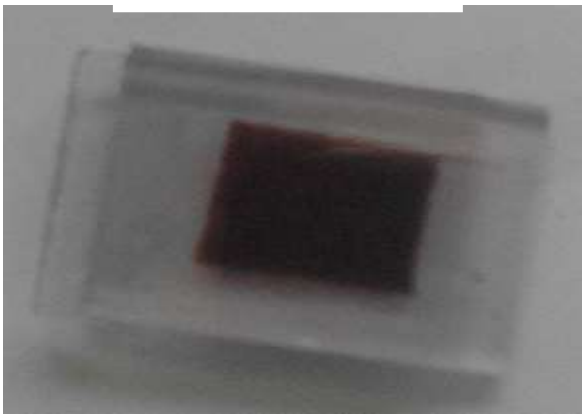

Appendix II: A Photograph of the I-V Measurement Setup in a Dark Room Showing the 450 W lamp, the Solar Meter and the I-V Measurement Circuit